

2

SEASAT III and IV

AD-A148 343

FILE COPY

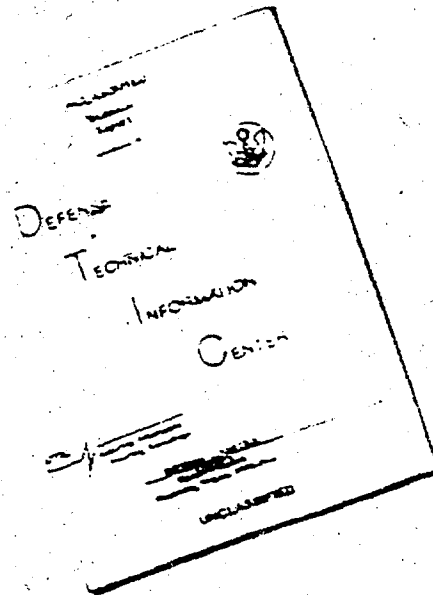
DTIC
CONNECTE
DEC 04 1984

MITRE

This document is based on information received from the MITRE Corporation, and is not to be distributed to the public.

84 11 21 060

DISCLAIMER NOTICE



THIS DOCUMENT IS BEST
QUALITY AVAILABLE. THE COPY
FURNISHED TO DTIC CONTAINED
A SIGNIFICANT NUMBER OF
PAGES WHICH DO NOT
REPRODUCE LEGIBLY.

REPRODUCED FROM
BEST AVAILABLE COPY

UNCLASSIFIED

SECURITY CLASSIFICATION OF THIS PAGE (When Data Entered)

REPORT DOCUMENTATION PAGE		READ INSTRUCTIONS BEFORE COMPLETING FORM	
1. REPORT NUMBER JSR-84-203	2. GOVT ACCESSION NO.	3. RECIPIENT'S CATALOG NUMBER	
4. TITLE (and Subtitle) SEASAT III & IV		5. TYPE OF REPORT & PERIOD COVERED	
7. AUTHOR(s) K. Case, C. Callan, R. Dasher, R. Davis, W. Munk, J. Vesecky, K. Watson, F. Zachariasen		6. PERFORMING ORG. REPORT NUMBER	
9. PERFORMING ORGANIZATION NAME AND ADDRESS The MITRE Corporation 1820 Dolley Madison Blvd. McLean, VA 22102		8. CONTRACT OR GRANT NUMBER(s) F19628-C-84-0001	
11. CONTROLLING OFFICE NAME AND ADDRESS		10. PROGRAM ELEMENT, PROJECT, TASK AREA & WORK UNIT NUMBERS	
14. MONITORING AGENCY NAME & ADDRESS (if diff. from Controlling Office)		12. REPORT DATE August 1984	13. NO. OF PAGES 150
		15. SECURITY CLASS. (of this report) Unclassified	
		15a. DECLASSIFICATION/DOWNGRADING SCHEDULE	
16. DISTRIBUTION STATEMENT (of this report) <div style="border: 1px solid black; padding: 5px; width: fit-content; margin: 10px auto;"> This document has been approved for public release and sale; its distribution is unlimited. </div>			
17. DISTRIBUTION STATEMENT (of the abstract entered in Block 20, if different from report)			
18. SUPPLEMENTARY NOTES			
19. KEY WORDS (Continue on reverse side if necessary and identify by block number)			
20. ABSTRACT (Continue on reverse side if necessary and identify by block number) <p>JASON continues its theoretical investigation of understanding the origin of the ship wakes seen by the SEASAT radar. The present effort incorporates the new experimental results from the Georgia Strait and Gulf of Alaska experiments. These experiments appear to rule out the internal wave hypothesis; they also seem to indicate that the Kelvin Wake (here defined in the most general sense to include non-linear processes as well as interactions with the turbulent wake) is rather different than conventional Kelvin wake theory would predict.</p> <p style="text-align: right;">(continued)</p>			

DD FORM 1 JAN 73 **1473**
EDITION OF 1 NOV 65 IS OBSOLETE

UNCLASSIFIED

SECURITY CLASSIFICATION OF THIS PAGE (When Data Entered)

UNCLASSIFIED

SECURITY CLASSIFICATION OF THIS PAGE (When Data Entered)

19. KEY WORDS (Continued)

20 ABSTRACT (Continued)

Nonetheless, a model which seems to be at least qualitatively reasonable can be constructed.

The generation of ship wakes (surface or internal) and their detection by radar is a complicated phenomenology involving various branches of physics, hydrodynamics and oceanography. Nevertheless, with the exception of the inner, small angle part of the Kelvin wake, we believe that the theoretical understanding of the problem is adequate to support the conclusions reached in the report.

DD FORM 1473 (BACK)
1 JAN 73

EDITION OF 1 NOV 68 IS OBSOLETE

UNCLASSIFIED

SECURITY CLASSIFICATION OF THIS PAGE (When Data Entered)

SEASAT III and IV

K. Case
C. Callan
R. Dashen
R. Davis
W. Munk
J. Vesecky
K. Watson
F. Zachariasen

August 1984

JSR-84-203



Approved for public release; distribution unlimited.

Accession For	
NTIS GRA&I	<input checked="checked" type="checkbox"/>
DTIC TAB	<input type="checkbox"/>
Unannounced	<input type="checkbox"/>
Justification	
By _____	
Distribution _____	
Availability Codes	
Dist	Avail and/or Special
A-1	

JASON
The MITRE Corporation
1820 Dolley Madison Boulevard
McLean, Virginia 22102

TABLE OF CONTENTS

	<u>PAGE</u>
INTRODUCTION AND SUMMARY	vii
1.0 SUMMARY OF THE EXPERIMENTAL SITUATION	1-1
2.0 INTERNAL WAVE HYPOTHESIS	2-1
3.0 KELVIN WAKE HYPOTHESIS	3-1
4.0 FUTURE EXPERIMENTS.....	4-1
APPENDIX A: SPECKLE NOISE	A-1
APPENDIX B: FIRST ORDER BRAGG CROSS SECTION: LIMITING CASES	B-1
APPENDIX C: NOTE CONCERNING THE PERSISTENCE OF A PATTERN OF SURFACE GRAVITY WAVES	C-1
APPENDIX D: CORRECTIONS TO SAR ESTIMATES OF V-WAKE ANGLES	D-1
APPENDIX E: SPECULAR POINT SCATTERING FROM COHERENT WAVE PACKETS.....	E-1
DISTRIBUTION	F-1

LIST OF ILLUSTRATIONS

<u>FIGURES</u>		<u>PAGE</u>
FIGURE 1-1a	V-wake in SEASAT (Rev. 407).....	1-2
FIGURE 1-1b	V-wake in Dabob Bay (DREP 8/3).....	1-3
FIGURE 1-1c	V-wake in Gulf in Alaska (Pass 006).....	1-4
FIGURE 1-2a	Radar Cross Section V-wake at 1 km Behind Ship.....	1-6
FIGURE 1-2b	Linear Intensity versus radar range across Quapaw Wake (Run 8-2). ERIM Optical Processor, 26 March 1984.....	1-7
FIGURE 2-1	The Farnborough Picture.....	2-11
FIGURE 3-1	X is drawn in a direction opposite to ship, Y is upwards.....	3-2
FIGURE 3-2	Definition plot.....	3-4
FIGURE 3-3	Geometric construction for SAR V's.....	3-5
FIGURE 3-4	The wing angles θ as a function of the look angle ψ	3-12
FIGURE B-1	Single radar aspect angle relative to the wake wave.....	B-7
FIGURE B-2	Radar orientation relative to the wake direction.....	B-10
FIGURE C-1	The decay time (3.2) due to viscous dissipation is shown as a function of wavelength.....	C-8
FIGURE C-2	The decay time (3.5) due to wind-sea interaction is shown as a function of wind speed for several wavelengths.....	C-10

LIST OF ILLUSTRATIONS (Concluded)

<u>FIGURES</u>	<u>PAGE</u>
FIGURE C-3	Limiting decay function (4.13) due to three-wave interactions is shown as a function of wind speed for several wavelengths..... C-21
FIGURE C-4	The decay time (4.34) due to three- and four-wave interactions is shown..... C-22
FIGURE C-5	The pattern spectral function..... C-30
FIGURE C-6	The pattern spectral function..... C-31
FIGURE D-1	Schematic illustration of scanning distortion for an aircraft SAR..... D-3
FIGURE D-2	Geometrical distortion in the slant-range imagery..... D-6
FIGURE E-1	Gulf of Alaska SAR--ship wake experiment showing characteristics to narrow angle wakes..... E-2
FIGURE E-2	Variation of classical Kelvin wavelength.... E-5
FIGURE E-3	Observations and models of the ocean's normalized radar cross-section..... E-16

LIST OF TABLES

<u>TABLES</u>	<u>PAGE</u>
TABLE 2-1	Radar Band Results..... 2-2
TABLE 2-2	Internal Wake Energies Computed by S. Borchardt (Dynamics Technology)..... 2-18
TABLE E-1	Sinusoidal Wave Parameters..... E-14

INTRODUCTION AND SUMMARY

There are essentially only two hypotheses for explaining the narrow V-wakes of ships seen by SEASAT. One is that the wakes are due to straining of ambient surface waves by the internal wave wake of the ship. The other is that the V-wakes are produced by the Kelvin wake of the ship. (Here the word Kelvin wake is used in the most general sense, and includes non-linear processes in the wake as well as possible interactions with the turbulent wake. It seems clear from the data that such non-linear effects are important in the near axis Kelvin wake).

As a result of the Georgia Strait experiment in the summer of 1983, and the Gulf of Alaska experiment in the spring of 1984, there is now a considerable amount of important new data available. The exercises at Georgia Strait consisted of two separate experiments. One, conducted at Knight Inlet where the buoyancy frequency is extremely high and the mixed layer is shallow, was explicitly designed to produce an internal wave wake. The observed (internal wave) wake was consistent with calculations based on standard internal wave theory and the measured density profile. The other experiment was done at Dabob Bay under conditions that are closer to those encountered in the open ocean. At Dabob Bay, a measureable internal wave

wake was neither expected nor observed. However the SAR did see narrow V - wakes. Direct observation of the the ocean surface clearly showed that these narrow V's were created by surface waves coming directly from the ship.

The Gulf of Alaska experiment took place in the open ocean in a region with an extremely deep mixed layer. The buoyancy frequency was essentially zero down to 100m, at which depth there was a peak of about 9 cycles per hour. No visible internal wave wake should be expected under those conditions, according to standard theory. Yet narrow V-wakes were again observed by the SAR.

The experimental results appear to rule out the internal wave hypothesis as an explanation of the SEASAT wakes. They also seem to indicate that the actual Kelvin wake, in the region of the SAR return, is rather different from what the conventional Kelvin wake theory would predict. This means that no good theory exists with which to explain the observed results quantitatively, both in the experiments and in the SEASAT images. Nevertheless, guided by the experimental observations, a model which seems at least qualitatively reasonable can be constructed. It is described in Section III of this report.

The Dabob Bay experiment observed narrow V-wakes during a period when the wind speed was low and there was little ambient wave activity. This is a special circumstance for two reasons: first the pattern in the Kelvin wake lasts longer and secondly the SAR directly sees the slopes in the Kelvin wake rather than their indirect effect on ambient ripples. Many (and perhaps even all) bright narrow wakes observed by SEASAT were also in calm seas. Our working hypothesis is that Kelvin wakes appear as narrow V's only when the wind speed is low. This hypothesis, which is strongly suggested by theory, receives further support from the Gulf of Alaska experiment. There, narrow V-wakes seem to disappear into the background as the wind speed increases.

The theoretical model described later in this report is applicable only in low wind speed conditions. Further work is required to understand the wind dependence; in particular the lifetimes of surface waves in varying wind conditions needs to be understood better. Some progress toward this goal is described later (see Appendix C).

The generation of ship wakes (surface or internal) and their detection by radar is a complicated phenomenology involving various branches of physics, hydrodynamics and oceanography. Nevertheless,

with one notable exception (discussed below), we believe that the theoretical understanding of the problem is adequate. In most cases careful calculations should be accurate to within a factor of two.

The exception is the inner, small angle part of the Kelvin wake. In this region the wake consists of short wavelength (typically tens of centimeters) waves travelling almost directly outward. At present there is no useful theoretical method for predicting the amplitude of these waves or even their gross pattern. Theoretical uncertainties are at least by an order of magnitude. This is in contrast to the situation for the outer part of the Kelvin wake near the cusp at 19.5° (half angle). Here it is possible to make rather accurate theoretical calculations. Essentially all the wave drag comes from the outer part of the wake.

Any theoretical attack, either analytic or numeric, on the small angle Kelvin wake is bound to be a difficult undertaking. However, the problem is a relative , unexplored one and research by qualified investigators should be encouraged.

For the record, the remainder of the theory (which is in good shape) includes (i) the generation of long wave length ($\lambda \gtrsim 100\text{m}$) internal waves by moving bodies (short wave length internal waves do

not penetrate the mixed layer and are irrelevant), (ii) modulation of surface ripples by internal waves or long surface waves and (iii) the general theory of radar scattering from the ocean surface, in the regime where the angle of incidence of the radar is not too near grazing and the modulation of surface ripples is relatively weak. This is the regime of interest for SEASAT and the other experiments discussed here. Under these conditions no measurements incompatible with the theory are known to us.

Part I of this report briefly reviews the experimental situation. Part II discusses the evidence regarding the Internal Wave hypothesis. Part III discusses the Kelvin Wake Hypothesis. It describes, first, the Dabob Bay results and a theoretical generalized Kelvin wake model suggested by them; and, second, some of the SEASAT and Gulf of Alaska observations in the light of the Kelvin wake hypothesis. Part IV suggests some future experiments.

There are also several appendices providing further details on various topics alluded to in the text.

1.0 SUMMARY OF THE EXPERIMENTAL SITUATION

The narrow V wakes which were first observed behind surface ships on SEASAT images have now been reproduced under much more controlled conditions in several experiments. There appears to be a remarkable uniformity among the results, (except for Knight Inlet, described below) which can be summarized by the following list of characteristics.

1. The V-wakes appear as narrow bright lines behind the ship. Figures 1-1a, 1-1b, and 1-1c give examples from SEASAT (Rev. 407), Dabob Bay (DREP 8/3), and the Gulf of Alaska (Ship pass 006, 03/13/84). The similarity is striking.
2. In all cases where the ship speed is known, the V-wake half angles θ (after various corrections are made) are consistent with the formula $\tan \theta = \pm C_g / U \cos \psi$, where C_g is the surface wave group speed appropriate to the SAR Bragg wavelength, ψ is the angle between the ship's course and the SAR flight direction, and U is the ship speed.



Figure 1-1a. V-wake in SEASAT.



Figure 1-1b. V-wake in Dabob Bay.



Figure 1-1c. V-wake in Gulf of Alaska.

3. The pattern of radar cross section change across the wakes is also very similar, as shown in Figures 1-2a and 2b (again for 407, DREP 8/3); the results in the Gulf of Alaska look similar. There are plots of $\Delta\sigma/\sigma$ (actually $\sqrt{\Delta\sigma/\sigma}$ for 407) across the wake about 1 km behind the ship. The peaks in $\Delta\sigma/\sigma$ are large ($\Delta\sigma/\sigma$ is about 10 in Dabob Bay and 4 in 407) and generally quite narrow (at most a few pixels).
4. The wake lengths vary, up to perhaps 20 km, and most if not all seem to occur at low wind speeds. In both Dabob Bay and the Gulf of Alaska wind speeds were known, and the V's disappeared for wind speeds above 2-3 m/sec. In SEASAT wind speeds were not known, but, judging by the dark backgrounds where tracks are seen, were apparently low when wakes were visible.
5. The wakes tend to disappear as the angle ψ between the SAR track and the ship track increases. Also, the V-wake angle θ seems, from Dabob Bay data, to decrease as ψ increases.

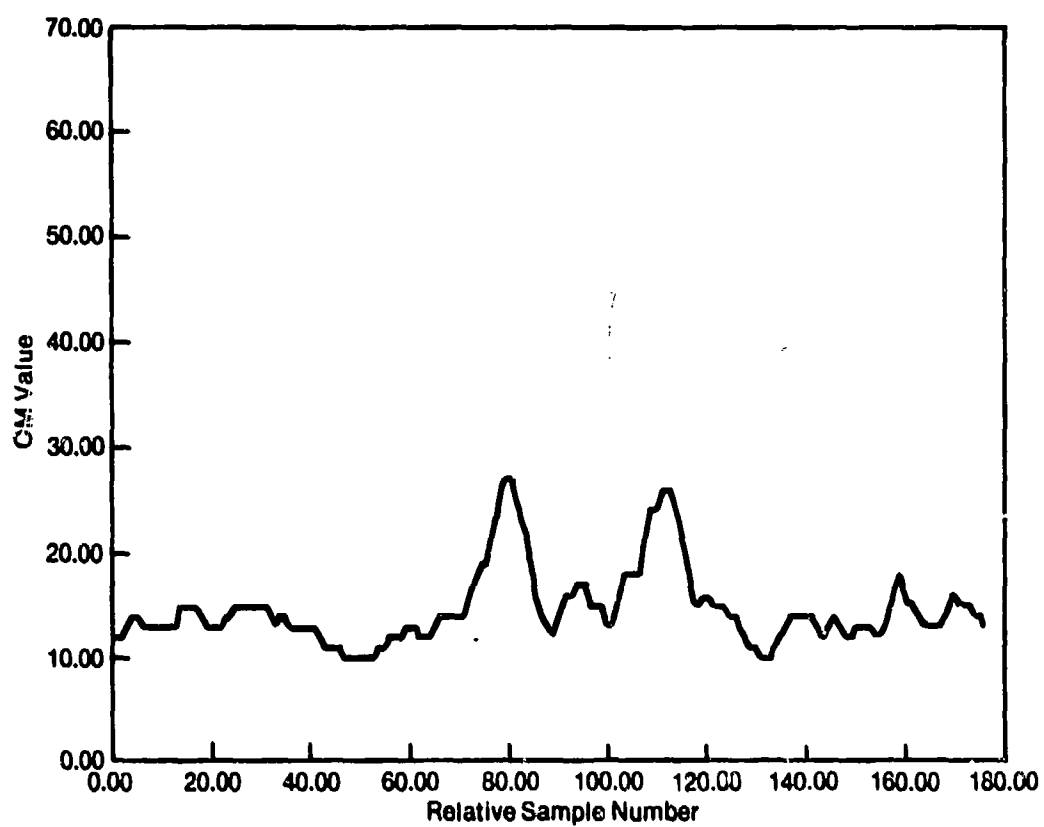


Figure 1-2a. Radar cross section across V-wake at 1km behind ship a) SEASAT Rev. 407.

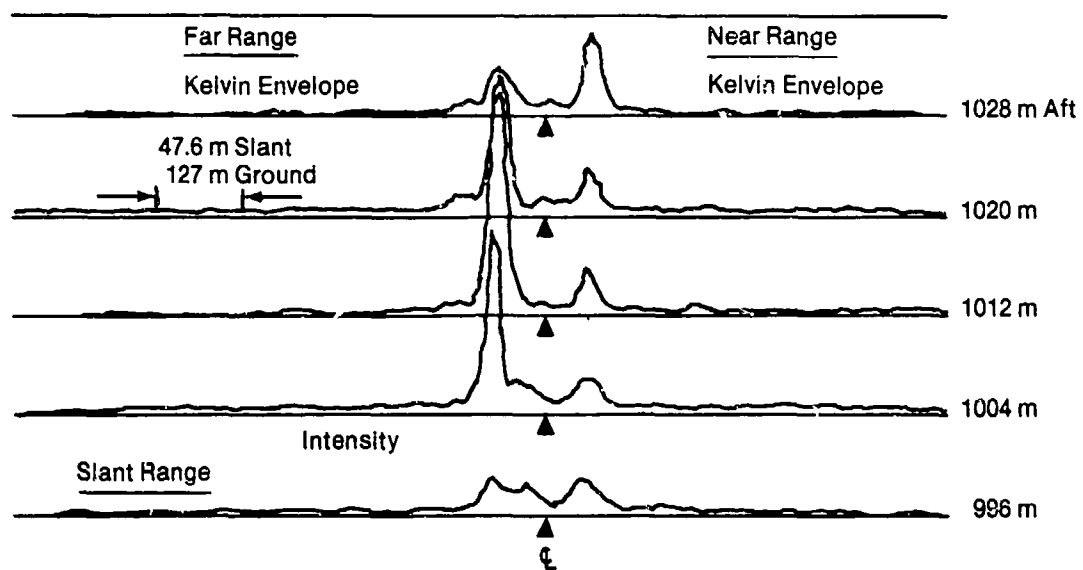
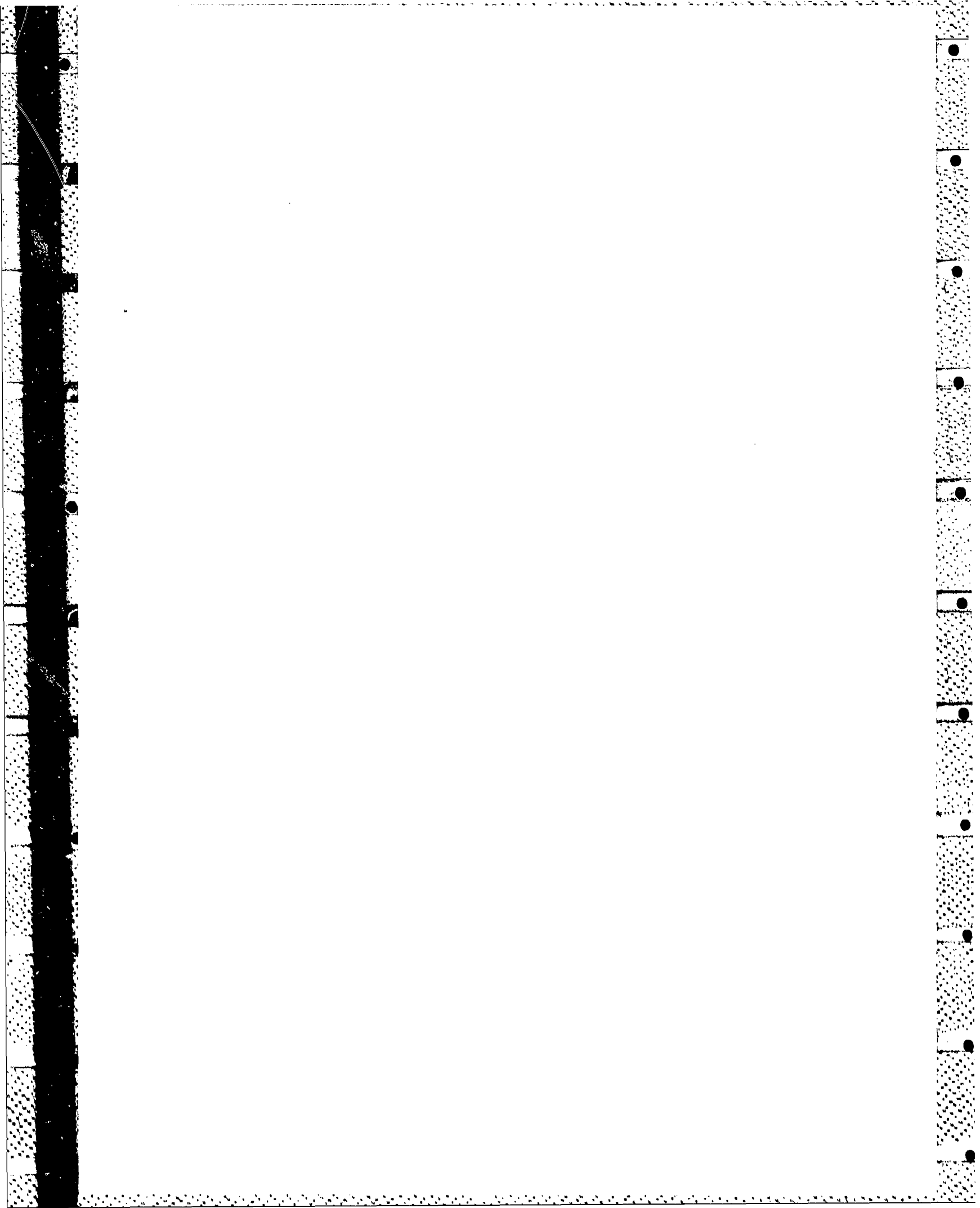


Figure 1-2b. Linear Intensity versus radar range across Quapaw Wake (Run 8-2).
ERIM Optical Processor, 26 March 1984.

6. The wakes (shown by Doppler offset in cases where ψ is large) are approximately stationary in the water rest frame, not in the ship rest frame: they do not travel with the ship.
7. At least some wakes show multiple crests (SEASAT Rev. 407 and perhaps some other SEASAT wakes; also, apparently, Gulf of Alaska wakes. (There is an indication of other peaks in the plot of $\Delta\sigma/\sigma$ vs. θ for Dabob Bay).
8. One case (Knight Inlet, DREP 10/8) looks rather different from the others. There are many crests, and the cross section modulation $\Delta\sigma/\sigma$ is very small. Both the V angle and the width of the pattern are much larger in the other cases. DREP 10/8, we remind the reader, was a slow ship (5 knots) moving in a very highly stratified region (peak buoyancy frequency of 69 cph at 5 m depth), for the deliberate purpose of exciting an internal wave wake.
9. The SAR look angle θ from vertical appears to be a crucial parameter. SEASAT was at 23° off vertical, and

most of the runs at Dabob Bay and in the Gulf of Alaska attempted to stay close to this. In one case, however, in the Gulf of Alaska θ was changed from about 30° , where the V wake was plainly visible, to about 50° , where the same wake entirely disappeared. It is worth noting that SIR A, a SAR flown on the space shuttle, saw surface ships but no narrow V wakes. Its look angle was also above 50° .

10. If the radar cross section is due to Bragg scattering, (at the SEASAT angle of 23° and at the lower angles in Dabob Bay and the Gulf of Alaska) the scattering is from surface waves of around 30 cm wavelength. In Dabob Bay the slope spectra across the wake were measured, and optical photographs of the wake were also taken. Neither of these measurements seems to show much enhancement over background at 30 cm wavelength (though both show considerable enhancement at larger wavelengths).



2.0 INTERNAL WAVE HYPOTHESIS

The hypothesis that ship generated internal waves are responsible for the narrow V-wakes observed behind surface ships by SEASAT appears to be incompatible with existing experimental results. This conclusion is based on the following observations.

A. Conventional theory predicts that the radar signature from straining of ambient surface waves by ship generated internal waves is too small by two or three orders of magnitude to be visible on SEASAT.

There are now several detailed numerical calculations of radar cross section modulations for several different pycnoclines and surface ships, appropriate to SEASAT Rev. 407, to Dabob Bay, to Knight Inlet, and to the Gulf of Alaska. All of these are pretty well consistent among themselves, and also agree reasonably well with earlier simpler theoretical calculations. Predictions of these calculations for various relevant quantities in the three situations are listed in Table 2-1.

B. Conventional theory is validated by the following sequence of experimental results.

TABLE 2-1

EXPT.	N (PEAK)	DEPTH OF PEAK	WATER DEPTH	
407 #1	9 cph	100 m	∞ m	
#2	19	25	∞	
#3	36	12	41	
DREP 8/3	35	15	160	
9/2	29	15	160	
10/8	69	5		
Gulf of Alaska (Ship pass 006, 3/13/84)	9	100	∞	
$\Delta\sigma/\sigma$ WIND SPEED	2 KTS	1	5	1
407 #1	--	--	.05	.02
#2	--	--	.10	.03
#3	.90	.50	.30	.10
DREP 8/3	.06	.02	--	--
9/2	.06	.03	--	--
10/8	--	--	1.4	.46
Gulf of Alaska (Ship Pass 006, 3/13/84)	--	--	.005	--

NOTE: The three 407 numbers are three different guesses as to the (unmeasured) profile.

a. As predicted by the theory, an internal wave wake was observed behind both QUAPAW and ENDEAVOUR in Knight Inlet (DREP 10/8). This wake is quantitatively reasonably consistent with the theoretical values for radar return and surface currents, as indicated in Table 2-1. Further, the observed geometrical pattern of the wake closely resembles the predicted pattern.

b. As predicted by the theory, no internal wave wake was observed in Dabob Bay. That the narrow wake seen in Dabob Bay is not an internal wave wake is indicated by the following observations.

1. The surface wave slopes, as measured directly from ENDEAVOUR, show an enhancement around the Kelvin wake wavelength as a function of wake angle from $19\frac{1}{2}^{\circ}$ down to about $2\frac{1}{2}^{\circ}$, at which point everything disappears, presumably due to wave-wave interactions among the very short waves, or to interactions with the turbulent wake. At the angle at which the V-wake is seen (2.6°), there is no evident enhancement over a wide band of surface wave wavelengths, such as one would expect to be produced by internal wave straining. Only the enhancement near the Kelvin wake wavelength is seen.

2. Measurement of the radar cross section across the narrow V-wake in Dabob Bay show very large (factor of 10) enhancements at $\pm 2.6^\circ$ from the wake axis. These enhancements are confined to a width of less than 22 m at 2 km behind the QUAPAW (the resolution used was 22 m).

The same feature was observed in the Gulf of Alaska. Large cross section enhancements occur within a single or few pixels when cuts are taken across the wake.

To produce a signal at $\pm 2.6^\circ$ behind a 7 m/sec ship, an internal wave must have a group speed of 35 cm/sec, or a phase speed in the Dabob Bay pycnocline of 44 cm/sec*. For the measured Dabob Bay pycnocline, this is quite fast, since the limiting phase speed is only 52 cm/sec.

At a phase speed of 44 cm/sec, the Dabob Bay pycnocline gives an internal wave frequency of 10^{-2} rad/sec and a wavelength of about 300 m. In the absence of nonlinear effects, an internal wave strains the surface over a distance of a quarter wavelength or so; for this case, that

* The dispersion relation for internal waves in the Dabob Bay pycnocline was furnished to us by Steve Borchardt of Dynatech.

is far larger than the observed upper limit of 22 m for the signal width. Conversely, for an internal wave of 100 m wavelength, the group speed is only 20 cm/sec, and the phase speed is only 34 cm/sec. These are much too slow to produce a signal at 2.6° .

For an internal wave to produce an effect over a more localized region than a quarter wave length requires that one invoke a more complicated surface wave-internal wave interaction mechanism, for which there seems to be no other evidence.

c. Much experimental information on natural internal waves exists. None of it appears to be incompatible with the standard theory, as described below.

One of the surprises of the SEASAT SAR experiment was that internal wave images were observed frequently along coasts, over sea mounts and even in the open ocean. This surprise stems from the fact that internal waves are essentially motions internal to the sea, having maximum particle displacements where the maximum vertical density gradients are found, 10's to 100's of meters below the

surface. Nevertheless, surface manifestations of internal waves are well observed by spacecraft and aircraft photography as well as SAR images. The large scale and unique shape of internal wave packets and the equally large scale SEASAT SAR images (100 km wide swath some 100's to 1000's of km long) account in some measure for the frequent observations.

The permanence of internal wave packets in SAR images has prompted a number of hypotheses to explain how internal waves couple to the surface roughness to which the radar waves are sensitive. Below we list several of these hypotheses:

1. Enhanced surface roughness in current convergence zones.
2. Surface current modulation of surfactants.
3. Surface current modulation of SAR image intensity via doppler effects.

4. Surface current modulation of wind generation of small surface waves (~30 cm wavelength).

Quantitative theory for these mechanisms is available for items 1 and 3 and we shall emphasize them in our discussion below.

Several SEASAT and aircraft SAR images of natural internal waves have been analyzed. In some cases corresponding surface and sub-surface measurements have also been made. Below we list several "experiments" in which SAR images of internal waves have been analyzed, noting location, reference and extent of surface measurements.

1. Georgia Straits (1978 & 1983): Aircraft and satellite SAR observations of internal waves plus extensive surface measurements were done in 1978 with further similar experiments involving aircraft SAR in 1983. (Hughes & Grant, 1978; Hughes, 1978 and Hughes & Gover, 1983).
2. Massachusetts Bay (1978): Four SEASAT SAR passes were analyzed in conjunction with buoy data from near Stellwagen Bank (Trask and Briscoe, 1983).

3. Gulf of California: Nine SEASAT SAR images were used to study internal waves generated by tides. Simple, non-linear theory allows estimates of internal wave amplitude and tidal losses. No surface observations were made (Fu & Holt, 1984).
4. JASIN (1978): Seventeen SEASAT SAR passes were made over the Joint Air-Sea Interaction (JASIN) experiment area west of Scotland in summer 1978. Internal waves were observed on numerous occasions and classified in terms of location, local wind speed, water depth, etc. Considerable surface and subsurface data was also collected. However, the SAR and in situ observations have not yet been analyzed together (Kasischke, et al, 1983; Levine et al., 1983 and Bagg, 1983).

We point out here that research concerning the observation of shallow water bathymetric features by SAR are relevant to the internal wave problem. Much of the same surface current-surface roughness coupling physics probably occurs in both cases. The source of surface currents is, of course, different in the two cases. Some recent papers are

published in the Proceedings of the Conference on the Future of Remote Sensing of the Troposphere and Oceans held in Israel in May 1984.

The primary question we ask of these data sets is, are they consistent with current understanding of the mechanism by which SAR can image surface manifestations of internal waves. By current understanding we refer to item 1 in the list of possible mechanisms above, namely that the internal wave induced surface currents interact with short (~ 30 cm) surface waves via weak hydrodynamic interaction. This leads to modulation of radar cross section (σ) by typical internal waves of ($\delta\sigma/\sigma$) on the order of unity. Although the data sets so far analyzed are not comprehensive (about a dozen cases quantitative comparisons have been made), they are generally in reasonable agreement with the above theory. There were observations of natural internal wave features during the 1983 Georgia Strait experiment which showed ($\delta\sigma/\sigma$) ~ 10 . However, these cases (one in particular called the "hum dinger") were exceptionally strong, internal bores, expected to be strongly non-linear.

d. Further support for the standard theory comes from an analysis of a Kelvin wake in a SEASAT image processed by RAE Farnborough, shown in Figure 2-1. The Farnborough picture shows a range-travelling ship plus an associated 39° (full angle) wake. The wake shows a pattern of transverse waves filling the interior of the 39° wedge, rather than the two very narrow bright rays visible on most SEASAT pictures.

V + Y

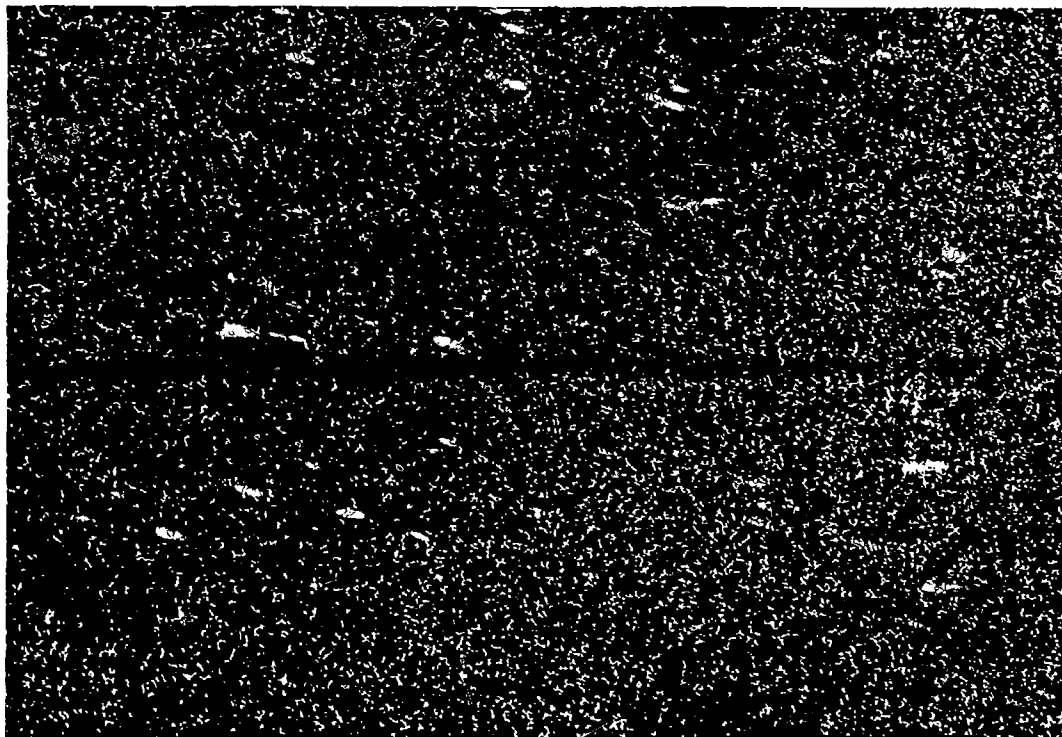


Figure 2-1. The Farnborough Picture.

The observed pattern seems to fit the structure of the standard Kelvin wake, suggesting that the water motions responsible for the radar cross-section modulation are nothing more or less complicated than the Kelvin wake. (It is interesting to note that the observation of a range travelling ship in the Gulf of Alaska (ship pass 010, 3/13/84) also shows the usual Kelvin wake but not the bright narrow V wake.) This gives us an opportunity quantitatively to test the hypothesis that the modulation is due to straining of an isotropic background of surface waves (or due to tilting such a background by a flow pattern produced by the ship).

Let us first establish some kinematic and geometrical facts about this picture. Horizontal scale is 38 m/mm on the picture. The transverse wave system has about 4 crests/10 mm or an apparent wavelength of 95 m. The wavelength of the transverse system behind a ship travelling at speed U is

$$\lambda = 2\pi \frac{U^2}{g}$$

The implied ship speed is $U = 12 \text{ m/s} = 24 \text{ knots (!)}$ A check on this comes from the displacement of the radar image of the ship from the head of the V. The vertical scale of the picture is 37 m/mm. The ship offset is 15 mm or $\Delta x = 550 \text{ m}$. The in-range component of the ship's velocity (from the picture, in fact, the ship appears to be travelling precisely in range) is

$$U = \Delta x \frac{V_{\text{SAT}}}{R} \frac{1}{\sin \theta_{\text{inc}}}$$

where V_{SAT} , R are the satellite's velocity and range. This gives $U = 12.7 \text{ m/s}$, which is consistent with the wavelength of the Kelvin wake.

Next, we want to estimate the amplitude of the Kelvin wave train in order to determine the strain and slope field which the radar is seeing. The far field transverse wave field can be fairly reliably calculated from slender ship theory at least far from the wake axis. The answer is, for a ship whose beam to length ratio is 1/10,

$$\text{displacement } \zeta = .6 \frac{U^2}{g} \sqrt{\frac{L}{x}} \cos \left(\frac{gx}{U^2} \right)$$

$$\text{slope } m_x = .6 \sqrt{\frac{L}{x}} \cos\left(\frac{gx}{U^2}\right)$$

$$\text{strain rate } \frac{\partial u_x}{\partial x} = \frac{g}{U} \sqrt{\frac{L}{x}} \cos\left(\frac{gx}{U^2}\right)$$

where x is the down track distance and L is the ship length.

The radar image suggests that the ship length is about 240 m. For $x = 6$ km, the maximum extent of the Farnborough picture, $\zeta \sim .25$ m and $m_x \sim 1$. Since slender ship theory probably over estimates the strength of the wake, these numbers should be decreased by a fudge factor of a few. Ideally, the wake could be computed using Carl Scragg's computer code.

Let us now consider the strain issue: The period of the transverse wave system is

$$T = \frac{2\pi U^2/g}{U} = 2\pi \frac{U}{g} = 7.7 \text{ sec}$$

The maximum strain in half a period is

$$\epsilon = \left(\frac{T}{2}\right) \left(\frac{\partial u_x}{\partial x}\right) = \left(\pi \frac{U}{g}\right) \left(.6 \sqrt{\frac{g}{U}} \sqrt{\frac{L}{x}}\right)$$

$$= (.6 \pi) \sqrt{\frac{L}{x}}$$

$$\approx .38 \quad @ x = 6000 \text{ m}$$

The strain modifies the ambient surface wave spectrum and we have to decide whether we are in the strain or strain rate regime (i.e., is the lifetime of the relevant surface waves long or short compared to the period of the Kelvin transverse waves). The Bragg wavelength is 30 cm and the period of such waves is

$$T = \sqrt{\frac{2\pi}{g}} \lambda = .44 \text{ sec}$$

The Kelvin wave period is 17 times as long. We will assume that this is small enough that decay of the surface wave is negligible and we are in the strain regime.

The empirical formula for radar backscatter modulation by a strain field $\epsilon(\vec{x})$, in the strain dominated regime, is

$$\frac{\delta\sigma(\vec{x})}{\sigma} = c \epsilon(x)$$

where c is nearly one. The strain field of the transverse Kelvin wake, according to the preceding paragraph, is

$$\varepsilon(x) \sim .38 \sqrt{\frac{6 \text{ km}}{x}} \cos\left(\frac{gx}{U^2}\right)$$

It is perfectly believable that the pattern in the Farnborough picture is due to a 40% intensity modulation. It would be good to have the digitized data so as to measure the intensity modulation.

The first order conclusion is that the picture of SAR returns as arising from strain modulation of wind generated ambient waves fits quantitatively what seems to be going on in the Farnborough picture. The key point is that in this picture it is clear that the Kelvin wake is directly responsible for the radar return and that there is a well developed ambient wave spectrum for the Kelvin wake to modulate. It would obviously be of great interest to combine Scragg's wake code with a radar cross-section model to obtain a quantitative prediction of the radar return to compare with the Farnborough picture.

e. To explain the SEASAT images by internal wave wakes requires that surface ships radiate internal waves much more efficiently than has been believed. One way to bound such a hypothetical mechanism is to compute the drag that would be associated with the internal wake. This has been done for selected cases with the results shown in Table 2-2. The power required to overcome IW drag (last column) is reasonable in all cases where the standard theory has been used (all rows except the bottom two). In the bottom two rows, the amplitude of the internal waves were (arbitrarily) multiplied by a factor of 7 and 10 to bring the radar cross section up to a level consistent with the SEASAT observations, giving 8,000 and 16,000 hp of IW drag. Since large commercial ships typically have power plants with 30,000 hp, we believe that IW drags of this magnitude are ruled out by experience. The possibility of bounding anomalous IW wakes by putting limits on drag should be studied in more detail.

TABLE 2-2

	B-V PROFILE	SHIP SPEED	ENERGY* IN INTERNAL WAVES	POWER* TO OVERCOME IW DRAG
DREP 9/2 QUAPAW DABOB BAY	Measured	16 kts	4.8 j/m	.05 hp
DREP 10/8 QUAPAW KNIGHT'S INLET	Measured	5 kts	1,924 j/m	6.5 hp
	(#1) Historical	16 kts	825 j/m	8.9 hp
	(#2) Optimistic (For IW's)	16 kts	15,000 j/m	160 hp
SEASAT REV. 407 CAPE CANAVERAL	Optimistic with source increased to get $\frac{\delta\sigma}{\sigma} = .7$	16 kts	730,000 j/m	7,800 hp
	Increased to get $\frac{\delta\sigma}{\sigma} = 1$	16 kts	1,500,000 j/m	16,000 hp

Table Caption: Internal wake energies computed by S. Borchardt (Dynamics Technology). Even with the "optimistic" profile the internal wave amplitudes for SEASAT Rev. 407 are too small to explain the observations. To obtain the last two rows the amplitudes are (arbitrarily) multiplied by 7 and 10 to get $\delta\sigma/\sigma$ of .7 and 1, respectively.

* Keeping 10 modes and wavelengths greater than 100m, the true IW drag is greater.

3.0 KELVIN WAKE HYPOTHESIS

This is the second serious contender for an explanation of the narrow V's. There are two obvious things to be said:

A Kelvin wake with its characteristic pattern of divergent and transverse waves does not look at all like a narrow V. But it is readily shown that in a classical Kelvin wake the wavenumber vector \underline{k} is a constant for constant wake angle θ (see Figure 3-1). Thus if the SAR is \underline{k} -selective (as it is in Bragg scattering) this would indeed lead to V-type signatures.

We do not understand the Kelvin wake theory for the interior wake (small θ) even one hundred years after publication of Lord Kelvin's classical paper. In the past the emphasis was on the outer 19.5° cusps which are important to the problem of wave drag.

Nevertheless we will try to interpret the Dabob results in terms of classical Kelvin wake theory. (The attempt turns out not to be successful, but it gives important clues.) The present assumption is that we see a classical Bragg reflection from the divergent waves of a classical Kelvin wake. (We believe this suggestion first came from NOSC.) But we must say at once that we believe that the SEASAT

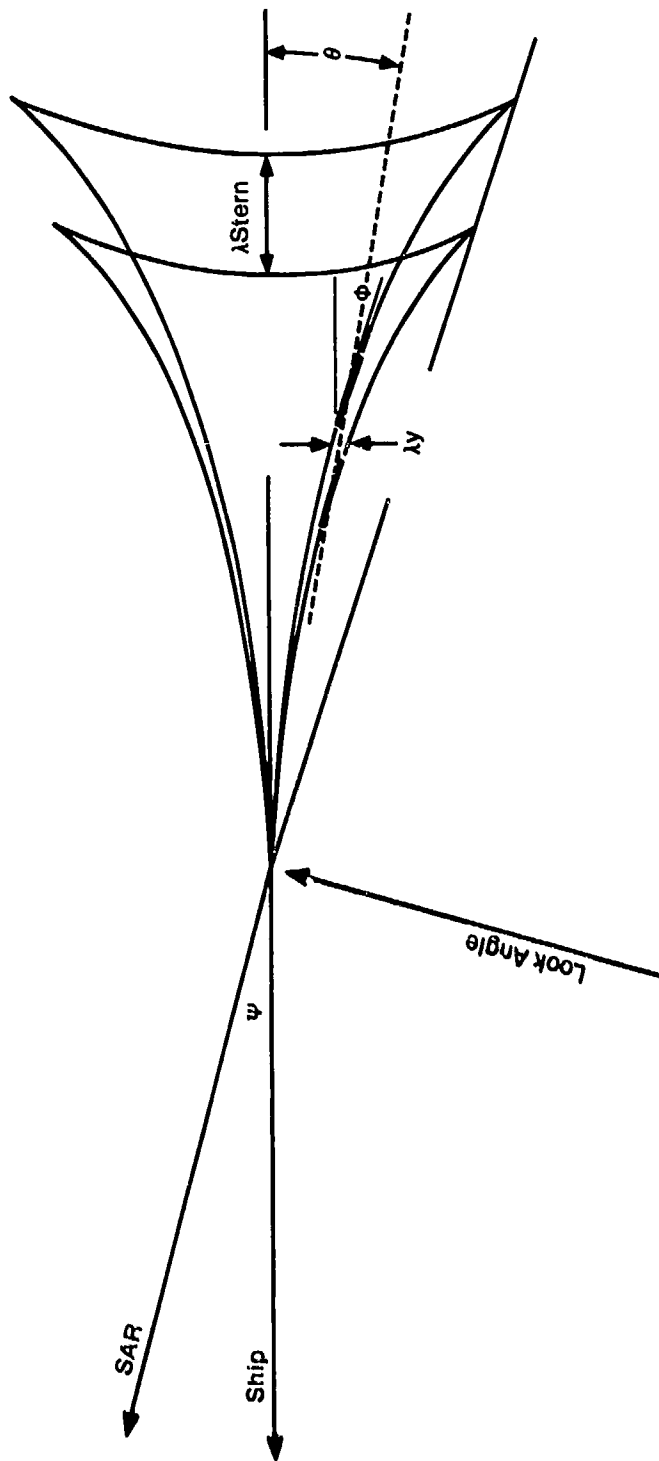
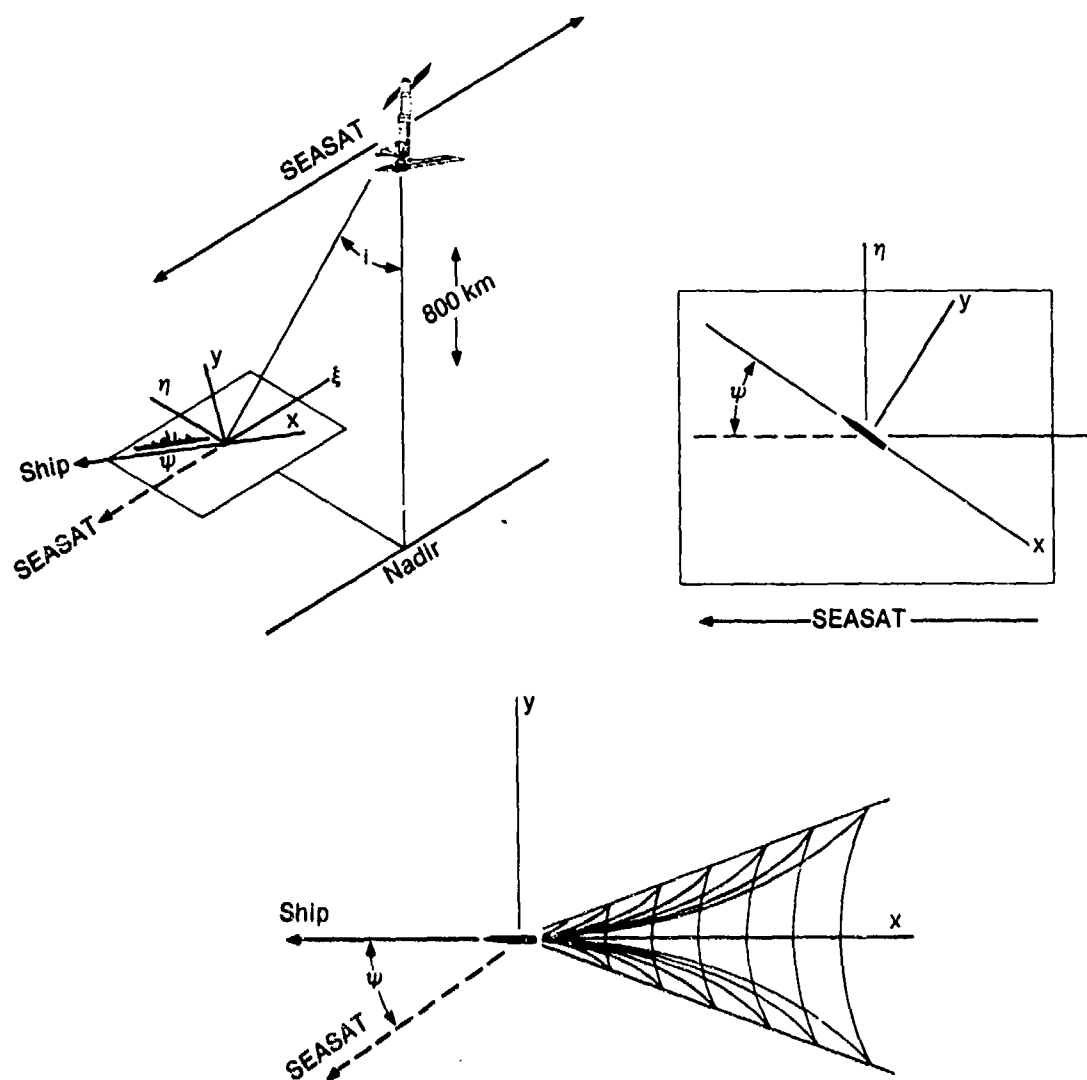


Figure 3-1. X is drawn in a direction opposite to the ship, Y is upwards. The turbulent wake is centered on the positive x-axis. The two wings of the V are characterized by two θ -values.

phenomenology is quite different for weak and strong winds (indeed it may not exist for strong winds), and for near-azimuth and non-azimuth travelling ships; Dabob Bay is representative only of the case of calm and more or less azimuthal ships.

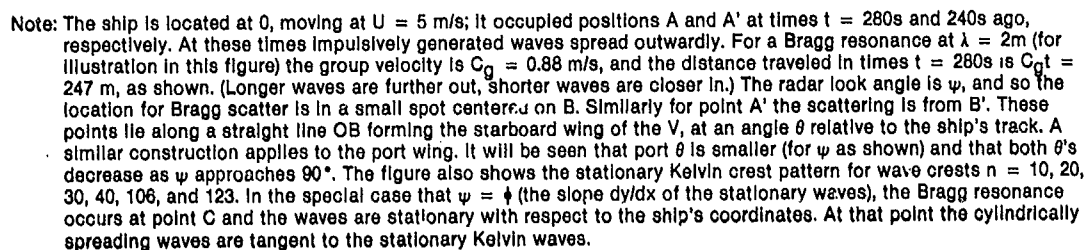
1. The angles are defined in Figure 3-2. SAR looks down at an angle i from the vertical. A ship in the field of view travels at an angle ψ to the right of the satellite course. The SAR coordinates ξ, η and the ship's coordinates x, y are shown; both are useful. Note that the ship is travelling in the negative x direction. The look angle (normal to the satellite course) is $\psi = 0, 180^\circ$ for an azimuth travelling ship, and $\psi = \pm 90^\circ$ for a range travelling ship.

2. The classical Kelvin solution consists of a series of waves $\eta = 1, 2, \dots$ which are stationary in a reference frame fixed to the ship. In this frame the water velocity is every where U in the positive x -direction. A wave crest $y(x)$ forms an angle $\tan \phi = dy/dx$ with the x -axis. The flow component normal to the crest is $U \sin \phi$, and the condition of stationarity is that this should be equal and opposite to the wave phase velocity C (see insert, Figure 3-3):



Note: The ship moves at an angle ψ to the right of SEASAT. Thus $\psi = 90^\circ$ corresponds to a positive rate-range, hence a negative Doppler, and in SEASAT coordinates ξ , y this leads to a relative ship displacement in the positive ξ direction.

Figure 3-2. Definition plot.



3-5

$$C = U \sin \phi \quad (1)$$

Loci of equal ϕ lie along a straight line which forms an angle θ with the wake axis (marked by the turbulent wake), with

$$\tan \theta = \frac{\tan \phi}{2 + \tan^2 \phi} \quad (2)$$

For small angles $\theta \approx \frac{1}{2} \phi$.

Each crest n has a divergent wave branch and a transverse wave branch; these join at the line of cusps where

$$\theta = \arcsin (1/3) = 19.47^\circ \quad (3)$$

We are concerned chiefly with the divergent waves. The wave length λ is relatively long near the cusp, and diminishes towards the interior (small θ and small ϕ) as

$$k = \frac{g}{U^2 \sin^2 \phi}, \quad \lambda = 2\pi/k. \quad (4)$$

The phase velocity $C = \sqrt{g/k} = U \sin \phi$ in agreement with (1), so that the relation (4) can be regarded as a purely geometric consequence of stationarity. The wave number components are

$$k_x = k \cos \phi, \quad k_y = k \sin \phi. \quad (5)$$

For the transverse wave at the axis we set

$$\phi = 90^\circ, \text{ hence } k = g/U^2, \text{ and } C = -U.$$

3. The Bragg condition states that backscatter is pronounced when the ocean wave crests are lined up normal to the look angle,

$$\phi_{\text{BRAGG}} = \psi \quad (6)$$

with a wave number (for first order Bragg).

$$k_b = 2 k_R \sin i. \quad (7)$$

Thus Bragg resonance from the Kelvin wake requires a very special combination of four independent experimental parameters (see Appendix B as well): the radar frequency f_R , the radar inclination i , the (relative) ship's course ψ and speed U . From (4), (6), and (7), this is

$$2k_R \sin i = \frac{g}{U^2 \sin^2 \psi},$$

where k_R is the radar wave number. In general this condition cannot be satisfied; in particular only one side of the classical Kelvin wake can be lined up properly so that only one side of a V-wake should be visible. We conclude that the classical Kelvin wake cannot explain the narrow V-wakes.

4. Suppose instead that the wave generation is variable. We can model it by a series of charges dropped from the stern of the moving vessel (not necessarily at regular intervals) (see also Appendix B). In the limit of zero interval between equal charges we recover the situation for a stationary phase solution. For definiteness Figure 6 has been drawn for $U = 5$ m/sec, and we now consider the situation 1.4 km and 1.2 km behind the ship, two points that were occupied by the ship 280s and 240s ago, respectively. From each of those two points (as from any other point) we have radial waves spreading outward, with group velocity C_g ; for deep water surface waves

$$C_g = \frac{1}{2} C = \frac{1}{2} \sqrt{g\lambda/2\pi} \quad (8)$$

The long waves are fast and out in front, the short waves are slow and nearer their point of generation. The circular arcs are drawn

for an assumed Bragg wavelength $\lambda = 2.00$ m which leads to $C = 0.353$ U. The arc to the left has a shorter radius, having been generated more recently. The conditions for Bragg resonance occur in the vicinity of the arcs at the points B, B' where the arcs are at right angle to the look direction ψ . For the triangle OAB we have $OA = Ut$, $AB = C_g t$, and hence

$$C_g \cos(\psi - \theta) = U \sin \theta,$$

or

$$\tan \theta = \pm \frac{\frac{C_g}{U} \cos \psi}{1 \mp \frac{C_g}{U} \sin \psi} \quad (9)$$

The two lines correspond to the two wings of the V; a positive θ corresponds to the starboard wing, a negative θ to the port wing.

The radar wave length and inclination determines

$C_g = [1/2 g \lambda_{\text{RADAR}} / \sin i]^{1/2}$; U is the ship speed, and ψ is the angle between satellite and ship course. Equation (9) then predicts the V-angles (Figure 3-3). We note a few special cases, designated by C,D,E along the circular arc:

E: Azimuth travelling ship, $\psi = 0$, $\tan\theta = C_g/U$

D: Maximum value of θ , $\psi = \theta$, $\sin\theta = C_g/U$

C: Stationary phase point, circular arc tangent to stationary phase crest. At this point the stationary phase condition (1) holds, $\sin\phi = \sin\psi = C/U = 2C_g/U$, and when this is substituted in (9) we recover the stationary phase result (2);

$$\psi = \phi, \tan\theta = \frac{\tan\phi}{2 + \tan^2\phi}$$

Presumably the strongest return comes from the vicinity of C, because it is here that sources very close to A interfere constructively.

Equations (9) predict some conditions which can be checked with SAR images:

1. The wing angles are constant and nearly equal at $\theta \approx \pm C_g/U$ for small to moderate values of ψ .
2. As $\psi \rightarrow 45^\circ$ there is a slight (but measurable) wing asymmetry.

3. For increasing ψ the V becomes increasingly narrower.
4. In SAR images (which uses Doppler for determining image coordinates) there is a combination of effects which are discussed in the next section.

5. For an increasing range-rate the Doppler is negative and the object is displaced in the direction of objects from which SAR is receding: that is towards positive ξ . Thus the ξ offset is proportional to

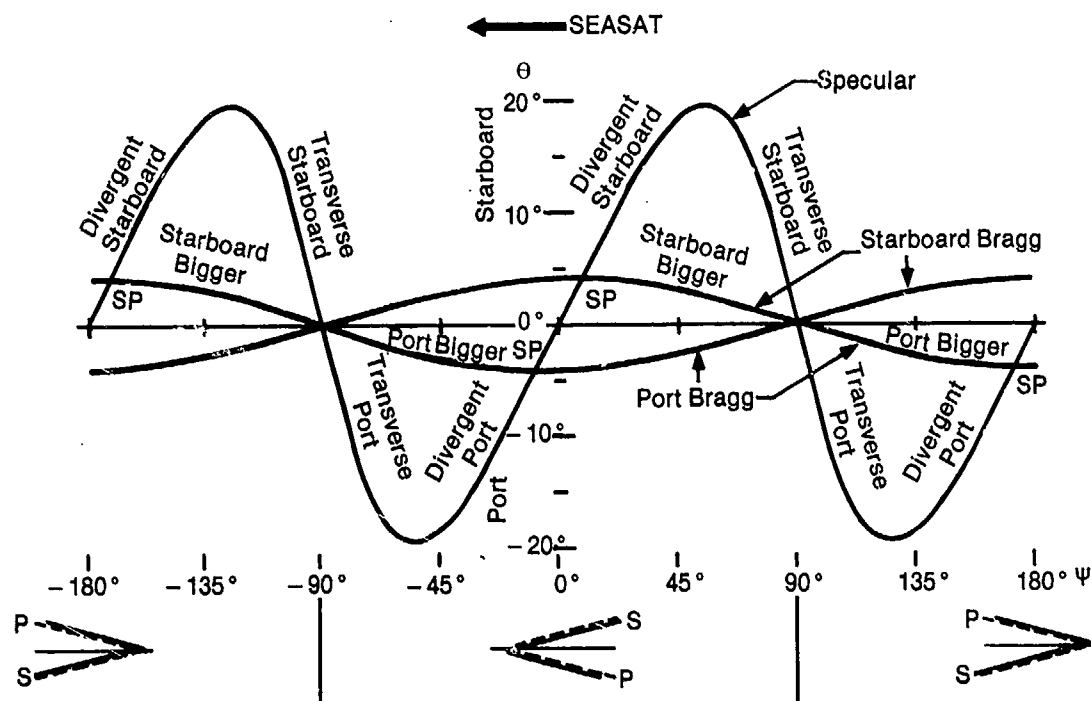
$U \sin\psi$ for the ship,

$\pm C \cos\psi$ for the S/P wings .

Accordingly wings and ships are offset equally if

$$\tan\psi = \pm C/U = \pm 2 C_g/U \text{ for S/P .}$$

This is shown in Figure 3-4.



Note: The Bragg curves are drawn for a ship speed $U = 7$ m/s, and a Bragg wavelength of 0.8 m, corresponding to $C_0 U = 0.069$. These curves are roughly at $\theta = \pm (C_0/U) \cos \psi$ for the starboard/port wings, so that θ varies as $\lambda + 1/2$ and U^{-1} . The wing angle difference is proportional to $\sin 2\psi$. For purely specular reflection (if it occurs), one can see only one wing or the other, depending on ψ . The specular points SP where the Bragg curves cross the specular curve, the Bragg scatterers are in stationary phase with the ship; for those special conditions one can expect strong signatures. Doppler offsets are indicated below (SAR travelling from right to left). The central line behind the ship represents the turbulent wake with assumed zero Doppler offset. The dashed lines give the positions of the Bragg wings without Doppler offset. For $\psi = 0$ there is no Doppler offset for the ship, and a slight Doppler offset for the wings (to the right for the starboard wing, to the left for the port wing), as indicated by the solid V. For $\psi = 90^\circ$ the Bragg wings coincide with the turbulent wake ($\theta = 0$) and are not offset, but the ship is offset to the right. At the SP point of $\psi = 8^\circ$, the starboard Bragg wing has the same Doppler offset as the ship, whereas at $\psi = -8^\circ$, the port Bragg wing has the same Doppler offset as the ship.

Figure 3-4. The wing angles θ as a function of the look angle ψ (positive for the starboard wing, negative for port).

There are some features of the observed V-wakes which are not clearly understood in terms of, or perhaps strain, the Kelvin wake hypothesis. We list these below.

(a) Multiple Crests

SEASAT Rev 407 shows wakes in which several lines appear to be visible in the wake. In the best picture, at about 7 km behind the ship, the wavelength between the two outer crests is about 200 m, and between the two inner crests about 100 m.

The version of the Kelvin wake theory described above does not obviously predict multiple crests. Perhaps they result from an interference pattern. A simple two point source model will give constructive interference at sufficiently small wake angles if the distance between the two point sources is less than a quarter of the transverse Kelvin wave wavelength, or less than about 7m. This is an exceedingly small number, and casts doubt on this idea.

One should keep in mind that under extreme circumstances internal wave wakes of ships can be seen. The very strong halocline in Knight Inlet is one such extreme case. Another is shallow water: if the water depth is only a few times the mixed layer depth very strong internal wave wakes can be produced.

Indeed, theoretical calculations by Dynatech using a measured (at a not too different time and place from the location of the ship) thermocline (407 #3; see Table 2-1) imply that the Internal wave wake in Rev. 407 could have been visible to SEASAT. This is partially because the peak buoyancy frequency was very large (36 cph) and shallow (12 m), and partially because of the shallow water depth (41 m). It is possible, therefore, that Rev. 407 actually is an internal wave wake, though the similarity of overall appearance between 407 and the other narrow V-wakes suggests that it is not. Knight Inlet, DREP 10/8, which no doubt actually is an internal wave wake, is very different in appearance from all of the others. Furthermore, there is the clear suggestion of multiple crests in the Gulf of Alaska as well. Thus it is likely that the Kelvin Wake model will have to come to grips with multiple crests.

(b) Wake Length

In SEASAT, some V-wakes are quite long, up to perhaps 20 km behind the ship. It is not at all clear that 30 cm surface waves produced by the ship can survive that long, even in conditions of fairly low wind. Evidently there needs to be more study of relaxation times for short wavelength surface waves, in various wind environments.

A 20 km long wake and a reasonable guess at ship speed suggests perhaps a half hour persistence time. At very low wind speeds (less than 2 m/sec or so) the lifetime of 30 cm surface waves is limited by viscosity. The e-folding time for wave amplitude is $\tau = (2 \nu k^2)^{-1}$ where ν is the kinematic viscosity and k is the surface wave wave number. For 30 cm waves this time is about 15 minutes. Since two e-foldings may well be visible, the observed lifetimes are not absurd, provided the wind speeds are really low. The lifetime degrades very rapidly as the wind velocity goes up; at a wind speed of 6 m/sec, for example, 30 cm waves have an e-folding time of order one second (see Appendix C.) Therefore, the Kelvin hypothesis is only tenable provided that all narrow V-wake observations occur under very low wind speed conditions.

We do not know the wind in pass 407; the dark background in the image suggests it could be quite low. In Dabob Bay, wind patches easily visible on the SAR are known to correspond to very low winds. Clearly more information on this question is needed. In both Dabob Bay and in the Gulf of Alaska, the narrow V-wakes disappear in regions of wind, and no wakes are visible at all at sea states of 3 and above.

4.0 FUTURE EXPERIMENTS

We believe that the experiments conducted up to now have demonstrated that the narrow V-wakes seen by SARs behind surface ships have nothing to do with internal wave wakes. We also believe that they have nothing to do with the classical Kelvin wake of a ship; instead we have suggested that the observations are compatible with a simple model (described in the previous section and in Appendix B) in which the near axis wake is as if it were produced by a series of charges dropped behind the ship. Exactly what this model has to do with a real ship remains unclear; presumably the near axis wake of a real ship is governed by complicated non-linear and turbulent flow along the ship sides as well as by the screw. The "charges" of the model may be related to regions of turbulence which are sporadically detached from the hull. To understand the details of all of this will be very difficult.

Nevertheless there are some experiments which can be performed to test further what is happening, and to further distinguish between the model and the internal wave hypothesis. These lie in varying Bragg wavelength of the radar. In the internal wave hypothesis, the radar backscatter is caused by the straining of the surface due to an internal wave; therefore the V-wake angle is

determined by the ratio of the speed of the ship to the internal wave speed. The V-wake angle should therefore be independent of the Bragg wavelength.

In the "depth charge model", on the other hand, the V-wake angle is determined by the ratio of the group speed of surface waves at the Bragg wave number to the ship speed; thus changing the Bragg wavelength will change the V-wake angle.

The Bragg wavelength can be changed either by changing the radar frequency f_R or by varying the radar incidence angle i . Since we know experimentally that the narrow V-wake disappears when i is too large (50° or more) the amount of variation which can be produced by changing i is limited. Nevertheless, changing i from 20° to 30° will change the group speed and the V-wake angle by the factor $(\sin 30^\circ / \sin 20^\circ)^{1/2} = 1.21$ which should be big enough to measure. Larger, and therefore more easily measured, changes can be made by changing f_R . However it is important not to use frequencies for which the corresponding surface waves are out of the gravity wave and into the capillary wave regime, since the physics may become quite different there.

In this context it is worth noting that one pair of ship

wake images taken simultaneously at L-band and at X-band already exists. (*) Both wavelengths show narrow V-wakes; that at L-band is much longer and appears wider than the one at X-band. The wavelength ratio is 7, so one would expect the ratio of wake angles to be $\sqrt{7}$. The observed ratio is about $\frac{5 \pm 1^0}{3.5 \pm 1}$. The wake at L-band is much longer than at X-band. Since the L-band wake extends off the picture, the wake length ratio cannot be determined. If the lifetime is purely due to viscous dissipation, the ratio should be 72. The length of visible track at X-band seems to be of order a kilometer. The ship speed can be determined from a clear transverse wave modulation of the wake; it is about 18 knots. Thus the X-band surface waves (whose wavelength is 4 cm) must therefore have lived some 100 seconds. This is an uncomfortably long time, and reinforces our earlier remarks about wake lengths.

(*) These were taken in July 1978 using an aircraft SAR. See R. Hammond, et. al., NOSC interim report on "Joint U.S. - Canadian Ocean Wave Investigation Report," p.44.

APPENDIX A

SPECKLE NOISE

Since detecting weak hydrodynamic modulation of SAR return is a central issue it is worth examining the intrinsic SAR noise, the dominant one being speckle noise.

The change of radar cross-section produced by particular hydrodynamic processes can not be predicted quantitatively nor is absolute calibration of SARs straightforward. Consequently, it is convenient to reference modulation of return to the average background return. Thus if I is a SAR intensity, $\langle I \rangle$ is an average which suppresses SAR noise but passes any modulation $\langle \delta I \rangle$ of the intensity and $\langle I \rangle_0$ is the average $\langle I \rangle$ of the background, then the most convenient measure of signal strength is the modulation index $\langle \delta I \rangle / \langle I \rangle_0$. Unfortunately, receiver noise makes it difficult to establish zero intensity so that measured intensity is often in error by a constant. Consequently, reported intensity ratios, particularly at low signal levels, may be in error.

If the SAR return is dominated by first order Bragg scattering the intensity, I , of a single radar look should be distributed as a chi-squared variable with two degrees of freedom; in particular the variance of I would equal the squared mean

$$\langle I^2 \rangle = \langle I \rangle^2.$$

Any hydrodynamic modulation must be strong enough to stand out above this speckle noise.

In the Seasat SAR images digitally processed by JPL, four radar views separated along the satellite track are averaged incoherently to produce an approximately 12m by 12m pixel. JPL images are typically digitized in units of amplitude, A , which is the square root of the energy unit I . If the energy in N independent looks are averaged the resulting intensity and amplitude obey the relations

$$\langle I^2 \rangle = \frac{1}{N} \langle I \rangle^2 \quad (A-1)$$

$$\langle A^2 \rangle = \frac{1}{N} \left[\frac{\Gamma^2(N+1)}{\Gamma^2(N+1/2)} - N \right] \langle A \rangle^2 \quad (A-2)$$

We have examined four 100-pixel regions from a JPL version of the Seasat Rev 407 image near Cape Canaveral in which a wake with

banded structure has been identified. The four regions were examples of unmodulated background found near this wake. Analysis indicates little interpixel correlation except that neighbor pixels separated in the along-track direction had correlation 0.6 ± 0.1 . Robust intensity and amplitude variance values were found:

$$\langle I'^2 \rangle = \frac{1}{[3.0 \pm 0.2]} \langle I \rangle^2 \quad (A-3)$$

$$\langle A'^2 \rangle = \frac{1}{[11 \pm 1]} \langle A \rangle^2 \quad (A-4)$$

Since the four-look pixels are correlated in the azimuth direction, so would the four individual looks in an average be correlated. Since a pixel is an average over less than four independent looks the speckle noise is more energetic than if four independent looks had been averaged. In fact (A-3, A-4) are consistent with (A-1, A-2) with $N = 3$. The observed azimuth correlation is somewhat larger than is easily explained by this slight reduction in the effective degrees of freedom.

In summary, the speckle noise in JPL processed Seasat SAR images is reasonably consistent with a first order Bragg scattering mechanism and a modest correlation of the fundamental looks from which the four-look pixels are obtained.

APPENDIX B

FIRST ORDER BRAGG CROSS SECTION: LIMITING CASES

Suppose we model the surface ship as a known but arbitrary pressure distribution $p_0(\vec{x}, t)$ on the water surface. Then the (linearized) surface displacement $s(\vec{x}, t)$ produced by this pressure is

$$s(\vec{x}, t) = \int \frac{d^2 k}{(2\pi)^2} e^{i\vec{k} \cdot \vec{x}} \frac{1}{\rho} \int_{-\infty}^t dt' \int d^2 \vec{x}' \sqrt{\frac{k}{g}} e^{-i\vec{k} \cdot \vec{x}'} p_0(\vec{x}', t') \exp\left\{ \frac{-i\sqrt{gk}(t-t')}{2i} e^{i\sqrt{gk}(t-t')} \right\} \quad (B-1)$$

The first order Bragg backscatter cross section is

proportional to $\sigma(t) = 2ik_v \int d^2 \vec{x} e^{-2i\vec{k}_H \cdot \vec{x}} s(\vec{x}, t)$ where the k_v and \vec{k}_H are the vertical and horizontal radar wave numbers, and the integral is taken over the illuminated area. For simplicity let us suppose the illuminated spot is defined by a Gaussian cutoff

$e^{-\alpha (\vec{x} - \vec{x}_0)^2}$ centered on a point \vec{x}_0 with a spot size of dimension $1/\alpha$.

Then we find

$$\sigma = -\frac{21k_v}{\rho} \sqrt{\frac{2k_H}{g}} \int_{-\infty}^t dt' \int d^2 \vec{x}' e^{-21\vec{k}_H \cdot \vec{x}'} p_0(\vec{x}, t')$$

$$\frac{1}{21} \left\{ e^{-i\sqrt{2gk_H}(t-t')} e^{-\alpha [\vec{x}_0 - \vec{x}' - \vec{C}_g(t-t')]^2} \right.$$

$$\left. - e^{i\sqrt{2gk_H}(t-t')} e^{-\alpha [\vec{x}_0 - \vec{x}' + \vec{C}_g(t-t')]^2} \right\} \quad (B-2)$$

Here $\vec{C}_g = \frac{1}{2} \sqrt{\frac{g}{2k_H}} \hat{k}_H$ is the group velocity of surface waves at the Bragg wave number $2\vec{k}_H$.

This expression is valid for an arbitrary pressure distribution $p_0(\vec{x}, t)$. Let us now look at some limiting special cases.

A. A moving point source.

Here $p_o(\vec{x}, t) = p_o \delta^2(\vec{x} - \vec{U}t)$ where \vec{U} is the ship velocity. Then

$$\sigma = \frac{2ik_v p_o}{\rho} \sqrt{\frac{2k_H}{g}} \int_0^\infty dt'' e^{2i \vec{k}_H \cdot \vec{U} (t''-t)} \\ \frac{1}{2i} \left\{ e^{-i\sqrt{2gk_H} t''} e^{-\alpha [(\vec{x}_o - \vec{U}t) + (\vec{U} - \vec{C}_g)t'']^2} \right. \\ \left. - e^{i\sqrt{2gk_H} t''} e^{-\alpha [(\vec{x}_o - \vec{U}t) + (\vec{U} + \vec{C}_g)t'']^2} \right\} \quad (B-3)$$

Aside from an overall phase $\exp(-2i \vec{k}_H \cdot \vec{U}t)$, σ is a function only of $\vec{x}_o - \vec{U}t$.

An (approximate) evaluation of (B-3) yields

$$\sigma = \frac{2i k_v p_o}{\rho} \sqrt{\frac{2k_H}{g}} \frac{1}{2i} \left\{ \sqrt{\frac{\pi}{\alpha (\vec{U} - \vec{C}_g)^2}} \right.$$

$$- \alpha (\vec{x}_o - \vec{C}_{gt})^2 \quad \alpha \frac{[(\vec{x}_o - \vec{C}_{gt}) \cdot (\vec{U} - \vec{C}_g)]^2}{(\vec{U} - \vec{C}_g)^2}$$

$$\frac{-1}{4\alpha} \frac{(2\vec{k}_H \cdot \vec{U} - \sqrt{2gk_H})^2}{(\vec{U} - \vec{C}_g)^2}$$

$$-1 \frac{(2\vec{k}_H \cdot \vec{U} - \sqrt{2gk_H}) (\vec{x}_o - \vec{C}_{gt}) \cdot (\vec{U} - \vec{C}_g)}{(\vec{U} - \vec{C}_g)^2}$$

$$- (\text{same with } \vec{C}_g \rightarrow -\vec{C}_g, \sqrt{2gk_H} \rightarrow -\sqrt{2gk_H}) \} \quad (B-4)$$

Evidently σ will be exponentially small unless both of the conditions

$$\vec{x}_0 - \vec{C}_g t \parallel \vec{U} - \vec{C}_g \quad (\text{B-5a})$$

and

$$2\vec{k}_H \cdot \vec{U} = \sqrt{2gk_H} \quad (\text{B-5b})$$

or both of the conditions

$$\vec{x}_0 + \vec{C}_g t \parallel \vec{U} + \vec{C}_g \quad (\text{B-5c})$$

and

$$2\vec{k}_H \cdot \vec{U} = -\sqrt{2gk_H} \quad (\text{B-5a})$$

are satisfied. When these are satisfied, we have

$$|\sigma| \approx \frac{k_v p_0}{\rho} \sqrt{\frac{2k}{g}} \sqrt{\frac{\pi}{\alpha}} \cdot \frac{1}{U}. \quad (\text{B-6})$$

The pair of conditions (B-5a, b) or (B-5c, d) indicate that the radar sees only waves having the Bragg wavelength and with crests oriented perpendicular to the radar look direction.

Let us choose the ship to be moving in the x direction. Then condition (B-5a) says that a return exists only at the wake angle θ satisfying

$$\tan \theta = - \frac{C_{gy}}{U - C_{gx}} = - \frac{C_g \cos \psi}{U - C_g \sin \psi}$$

where ψ is the angle between the satellite track and the ship track;
or, for $C_g \ll U$, and therefore θ small,

$$\theta = - \frac{C_g}{U} \cos \psi ,$$

(the other arm of the V-wake comes from (B-5c)) which is the usual Bragg selected wake angle. Condition (B-5b), however, also requires that

$$2k_{Hx} U = \sqrt{2gk_H}$$

This is the Kelvin wake condition; it requires that the radar be oriented perpendicular to the Kelvin wake wave crests. This will be the case if

$$\frac{k_{Hx}}{k_{Hy}} = \frac{-2 C_{gy}}{U - C_{gx}} = - \frac{2 C_g \cos \psi}{U} ;$$

therefore only for a single radar aspect angle relative to the wake wave is there a return. (See Figure B-1.) In particular, therefore, only one arm of the Kelvin wake will be visible.

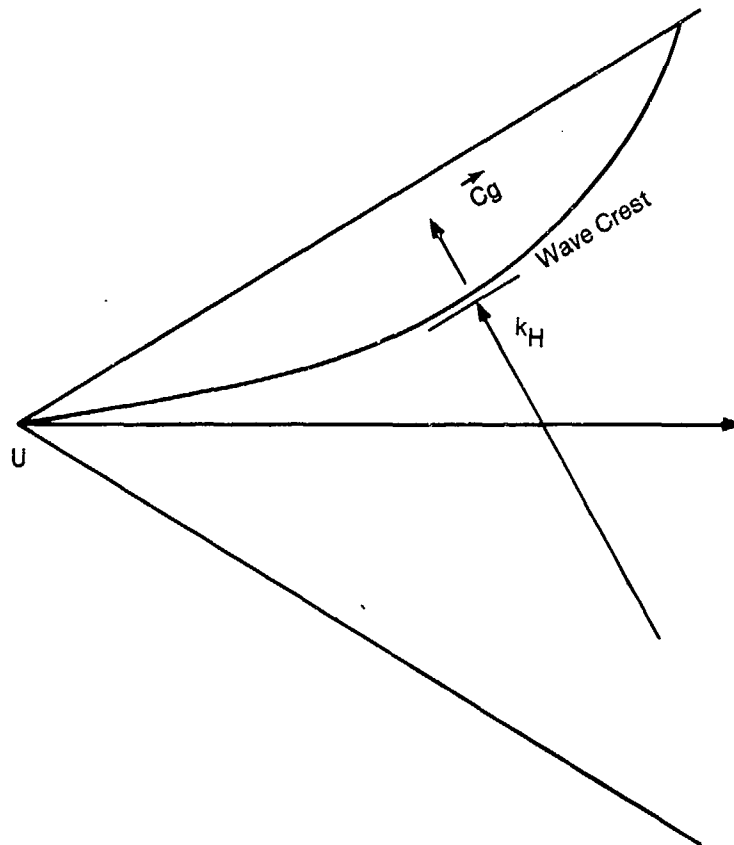


Figure B-1. Single radar aspect angle relative to the wake wave.

B. A line of fixed point sources.

Next let us take the source pressure to be

$$p_o(\vec{x}, t) = p_o \sum_n \delta^2(\vec{x} - \vec{U} n \tau) \delta(t - n\tau) e^{i\phi_n}$$

representing a line of stationary (in the water) instantaneous incoherent sources. (This is the simple depth charge model described in Section III). Now we find

$$\begin{aligned} \sigma &= \frac{21 \text{ kv } p_o}{\rho} \sqrt{\frac{2k_H}{g}} \sum_n e^{-2ik_H \cdot \vec{U} n \tau} e^{i\phi_n} \theta(t - n\tau) \\ &\frac{1}{2H} \left\{ e^{-i\sqrt{2gk_H}(t-n\tau)} e^{-\alpha [\vec{x}_o - \vec{U} n \tau - \vec{C}_g(t-n\tau)]^2} \right. \\ &\quad \left. - (\vec{C}_g \rightarrow -\vec{C}_g, \sqrt{gk_H} \rightarrow -\sqrt{gk_H}) \right\} \end{aligned} \quad (B-7)$$

Suppose the spacing between sources is big enough so that only a single term, say $n = n_o$, in the sum contributes for a given spot location \vec{x}_o and time t . Then

$$|\sigma| = \frac{k_v p_o}{\rho} \sqrt{\frac{2k_H}{g}} \quad (*)$$

and we must have the constraint $\vec{x}_o \pm \vec{C}_g t = (\vec{U} \pm \vec{C}_g) n_o \tau$.

(*) Keep in mind that P_o here has different dimensions from the P_o in the limit described in Eq. B-6.

Thus we obtain returns at wake angles.

$$\tan \theta = \mp \frac{\vec{C}_g \cos \psi}{U \pm C_{gx} \sin \psi}$$

or, for small angles,

$$\theta \approx \pm \frac{C_g}{U} \cos \psi$$

The wake angles allowed are the same as in Case A (constraint B-5a or B-5c) but there is now no constraint on the radar orientation relative to the wake direction; (see Figure B-2) there is a return for any direction of \vec{k}_H .

If the spacing between sources is much less than the spot size, and if the phases ϕ_n are all the same so that the sources are coherent, then this situation reduces to Case A, the normal Kelvin Wake. Any intermediate case, or a case with any other kind of pressure distribution in space and time, is described by Eq. (B-2).

Under some circumstances, second and higher order Bragg scattering can be important. The second order Bragg cross section is calculated in other JASON reports.

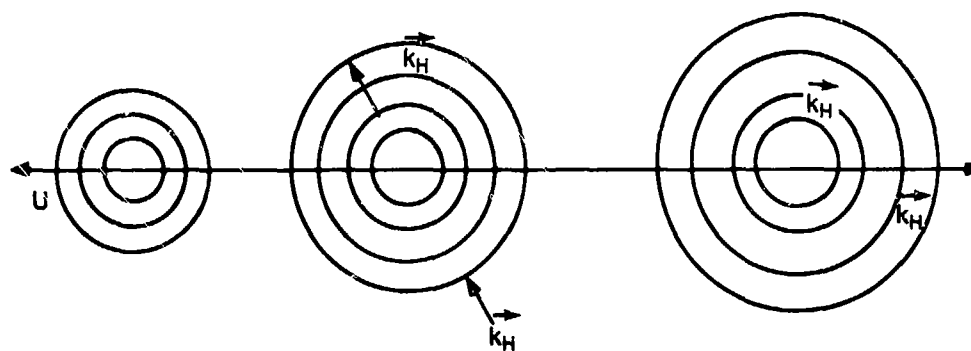


Figure B-2. Radar orientation relative to the wake direction.

APPENDIX C

NOTE CONCERNING THE PERSISTENCE OF A PATTERN OF SURFACE GRAVITY WAVES

1. INTRODUCTION

The imaging of surface ship Kelvin wakes by a SAR raises an interesting question: How long will a given "pattern" of surface waves persist? Under conditions of light wind and low sea state the Kelvin wake of a vessel may be seen to persist astern for some kilometers. Under more robust sea conditions the wake persistence seems to be greatly reduced. In this note we shall discuss aspects of the decay of such a "pattern". This is a complex phenomenon and cannot be exhaustively addressed here.

Deterministic mechanisms, such as linear wave propagation and the interaction with known large scale currents, can distort a wave pattern. This, however, is in principle predictable and will not be considered as "pattern decay". Stochastic mechanisms, such as interaction of the pattern with wind and ambient sea, do lead to a genuine decay of the wave pattern.

We shall be concerned only with patterns formed by gravity waves. Capillary wave decay is expected to occur at time scales too short to be of interest here.

There are evidently several mechanisms that contribute to wave "pattern decay". Viscous dissipation seems to be the simplest of these. Wind-wave interaction, while physically complex, is phenomenologically modelled as a simple exponential pattern decay. These mechanisms are reviewed in Section 3.

Nonlinear hydrodynamic interactions of the "pattern" with ambient surface waves provide other decay mechanisms. In the terminology of wave-wave weak interaction theory, both "three-wave" and "four-wave" interactions must be considered. It is well-known that the three-wave interactions do not admit resonant frequency conditions. We shall see that these lead to only partial pattern decay. Only if this decay brings the signal-to-noise level below the threshold for detectability, can we consider the pattern destroyed. The four-wave interactions act on a slower time scale than do the three-wave interactions, but lead to total decay of the pattern (according to weak interaction theories).

The role of three and four-wave interactions is discussed in Sections 4, 5, and 6. In Section 4 we discuss the decay with

respect to an amplitude matched filter in the space time domain. In Section 5 we describe the evolution of the power spectrum of the pattern due to three-wave interactions. In Section 6 we make some estimates of the spectral evolution resulting from four-wave interactions.

2. DESCRIPTION OF THE DECAY PHENOMENA

In a specified "rectangular area of ocean" we use a Fourier expansion for the surface wave displacement $\zeta(\underline{x}, t)$ ($\underline{x} = x, y$, a vector in the plane of the quiescent ocean surface):

$$\zeta(\underline{x}, t) = -\text{Im}[Z(\underline{x}, t)]$$

$$Z(\underline{x}, t) = \sum_{\underline{l}} b_{\underline{l}} \exp[i(\underline{l} \cdot \underline{x} - \omega_{\underline{l}} t)] . \quad (C-1)$$

Here $\omega_{\underline{l}} = (g l)^{1/2}$. In the approximation that the waves are linear and not forced, the $b_{\underline{l}}$ are constants. In general, $b_{\underline{l}}(t)$ is time dependent.

We shall suppose that (C-1) refers to the ambient sea. For the "pattern waves" we take as a special case of (C-1)

$$\zeta_p(\underline{x}, t) = -\text{Im}[Z_p]$$

$$Z_p = \sum_{\underline{k}} B_{\underline{k}} \exp[i(\underline{k} \cdot \underline{x} - \omega_k t)] \quad (C-2)$$

We shall suppose that the $B_{\underline{k}}$ are amplitudes (they determine the pattern) at some reference time, say $t = 0$. The ambient sea will here be presumed as linear, so the $b_{\underline{l}}$ are constants. Over an ensemble of realizations of the ocean surface the $b_{\underline{l}}$ will be considered to be uncorrelated Gaussian variables. The ensemble averaged spectrum Ψ of vertical displacement is

$$\int \Psi(\underline{l}) d^2 l = \sum_{\underline{l}} \frac{1}{2} \langle |b_{\underline{l}}|^2 \rangle \quad (C-3)$$

In this paper we shall use a Pierson-Moskowitz (1964) spectrum for the ambient sea:

$$\Psi(\underline{l}) = \left(\frac{\eta}{l^4}\right) \exp\left[-\left(\frac{l_0}{l}\right)^2\right] G(\theta) ,$$

$$\eta = 4 \times 10^{-3} , \quad l_0 = 8.4 / W^2 \quad (C-4)$$

Here W is the wind velocity expressed in m/sec, l_0 is in m^{-1} , and θ is the angle between \underline{l} and \underline{W} . We shall specify models of $G(\theta)$ later, but now note the normalization

$$\int_{-\pi}^{\pi} G(\theta) d\theta = 1 . \quad (C-5)$$

For the pattern waves we introduce the Wigner (1932) correlation function

$$\Gamma_p(\underline{r}, \underline{x}, t) = \frac{1}{2} \langle Z_p(\underline{x} - \underline{r}/2, t) Z_p^*(\underline{x} + \underline{r}/2, t) \rangle \quad (C-6)$$

Here $\langle \dots \rangle$ represents an ensemble average over the ambient sea, as in (C-3). The spectrum of vertical displacement is*

$$\Psi_p(\underline{k}, \underline{x}, t) = \int \Gamma_p e^{i \underline{k} \cdot \underline{r}} d^2 r / (2\pi)^2 . \quad (C-7)$$

The spectrum of wave action F_p and the energy spectrum E_p (both per unit area of ocean) are related to (C-7) by the expressions

$$F_p = \left(\frac{g \rho_0}{\omega_k} \right) \Psi_p = E_p / \omega_k . \quad (C-8)$$

Here ρ_0 is the density of sea water.

The Hasselmann (1967) evolution equation for F_p is of the form

$$\frac{\partial F_p}{\partial t} + \dot{\underline{x}} \cdot \nabla_{\underline{x}} F_p = S_{nl} + S_v + S_w . \quad (C-9)$$

*It is assumed, of course, that ψ varies slowly over distances comparable to pattern wavelengths of interest.

Here

$$\dot{\tilde{x}} = \nabla_k \omega_k ,$$

and S_{nl} , S_v , and S_w represent the effects of wave-wave interactions, viscosity, and wind, respectively. In (2.9) we are omitting interaction with large scale surface currents.

3. EFFECTS OF VISCOSITY AND WIND

Viscosity will lead to exponential damping of the pattern waves. In the notation of (C-9) this is expressed as (Phillips, 1977)

$$S_v = -\beta_v F_p ,$$

$$\beta_v = 4\nu k^2 , \quad (C-10)$$

where $\nu \hat{=} 1.1 \times 10^{-6} \text{ m}^2/\text{sec}$ is the kinematic viscosity of sea water. The decay time

$$T_d(\nu) \hat{=} \beta_v^{-1} \quad (C-11)$$

is shown as a function of wavelength

$$\lambda = \frac{2\pi}{k}$$

in Figure C-1.

The rate of wind induced growth for surface waves has recently been reviewed by Plant (1982). He concludes that for the growth rate of small amplitude waves,

$$S_w = -\beta_w F_p \quad (C-12)$$

in (C-9). Here

$$\beta_w = 0.04 u_*^2 k^2 \cos \theta / \omega_k, \quad (C-13)$$

where u_* is the friction velocity of the wind and θ is the angle between \underline{k} and \underline{w} .

It seems plausible for our purposes to interpret

$$T_d(w) \equiv \beta_w^{-1} \quad (C-14)$$

as a pattern decay time.

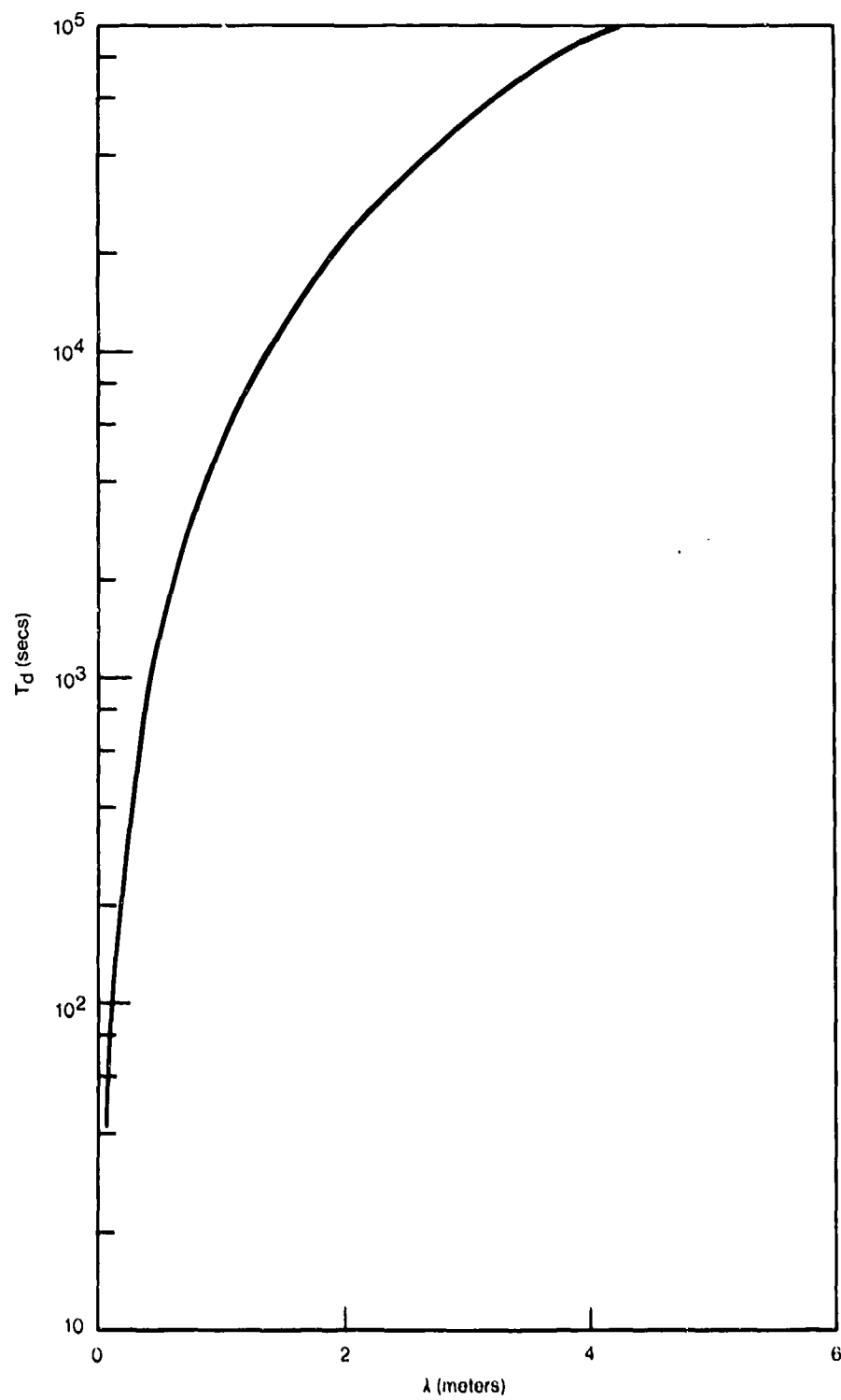


Figure C-1. The decay time (3.2) due to viscous dissipation is shown as a function of wavelength.

To evaluate (C-14) we use the analysis of Garratt (1977) to relate u_* to the wind speed W . The resulting time $T_d(w)$ is shown in Figure (C-2) as a function of W for several wavelengths λ and angle $\theta = 0$.

We note from Figures (C-1) and (C-2) that for $W > 2$ m/sec that $T_d(w) < T_d(v)$ when $\lambda > 0.1$ m.

4. DECAY FROM A PREDICTED PATTERN

One simple descriptor of pattern decay is given by the correlation function

$$\Gamma_o(t) = \langle P\{\zeta_p(\underline{x}, 0; t) \zeta_p(\underline{x}, t)\} \rangle \quad (C-15)$$

Here $t = 0$ is considered to be the reference time at which the pattern is first observed. The quantity

$$P\{\zeta_p(\underline{x}, 0; t)\}$$

represents the predicted field at t , given the initial field

$\zeta_p(\underline{x}, 0)$. The prediction is to be obtained using known deterministic phenomena which may distort the pattern. For example,

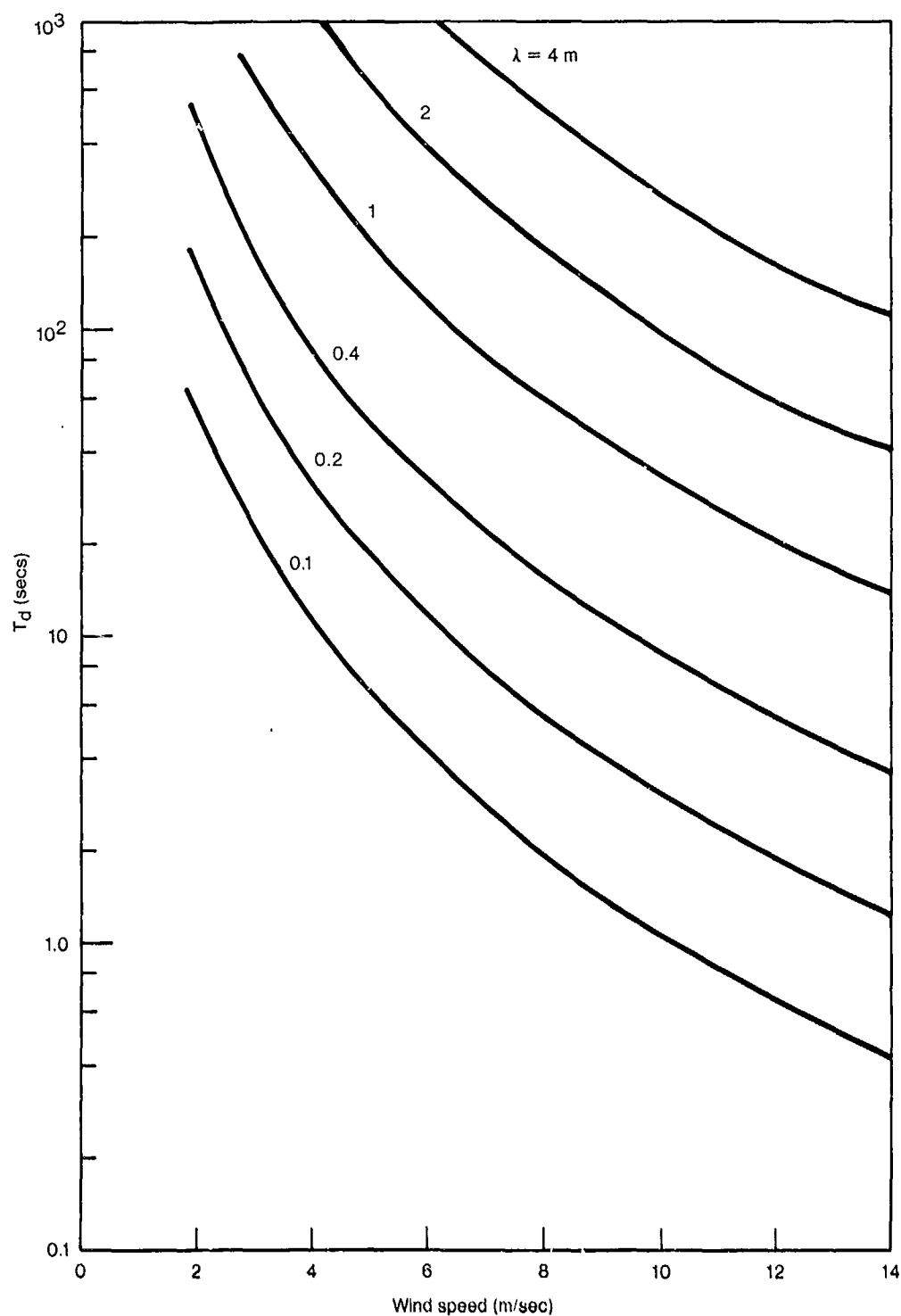


Figure C-2. The decay time (3.5) due to wind-sea interaction is shown as a function of wind speed for several wavelengths.

if linear wave propagation is the only deterministic phenomenon, then

$$P \{ \zeta_p(\underline{x}, 0); t \} = -I_m \{ \sum_{\underline{k}} B_{\underline{k}}(0) \exp[i(\underline{k} \cdot \underline{x} - \omega_{\underline{k}} t)] \} \quad (C-16)$$

where $B_{\underline{k}}(0)$ is the value of $B_{\underline{k}}$ at $t = 0$.

In this paper we shall assume that (C-15) applies in evaluating (C-15). Then it is sufficient to calculate the set of correlations

$$\gamma_{\underline{k}\underline{k}'}(t) = \langle B_{\underline{k}}(t) B_{\underline{k}'}(0) \rangle = \langle B_{\underline{k}}(t) \rangle B_{\underline{k}'}(0) \quad (C-17)$$

We shall refer to a given Fourier amplitude in the pattern as a "test wave".

Under certain conditions we might expect $\langle B_{\underline{k}} \rangle$ to be determined from a Langevin equation of the form

$$\frac{d}{dt} \langle B_{\underline{k}} \rangle = -v(\underline{k}) \langle B_{\underline{k}} \rangle, \quad (C-18)$$

where $v(\underline{k})$ is the Langevin "rate constant". In this case we would evaluate (C-17) as

$$\gamma_{\underline{k}\underline{k}'} = B_{\underline{k}}(0) B_{\underline{k}'}(0) \exp[-v(\underline{k})t] \quad (C-19)$$

We shall see that four-wave interactions, with frequency resonance, lead asymptotically to equations of the form (C-18) and (C-19).

As a first illustration of (C-15) and (C-16) we consider the advection of a test wave "k" due to the surface current $\underline{U}(\underline{x}, t)$ of the ambient waves. This current is of the form

$$\underline{U}(\underline{x}, t) = \sum_{\underline{l}} \Sigma(\frac{1}{2}) \hat{l} \omega_{\underline{l}} \{ b_{\underline{l}} \exp[i(\underline{l} \cdot \underline{x} - \omega_{\underline{l}} t)] - c.c. \} \quad (C-20)$$

using the notation of (C-1). We have assumed that the ambient waves are linear, so the $b_{\underline{l}}$ are constant. We shall also assume that

$$l \ll k, \quad (C-21)$$

or that the wavelength of the test wave is small compared with that of those ambient waves which are of most importance for pattern decorrelation. This assumption can be tested for verification when we evaluate the decay using the spectrum (C-4).

If the test wave is advected with the local velocity \underline{U} we use (C-21) to write

$$B_{\underline{k}}(t) \approx B_{\underline{k}}(0) \exp[-i \underline{k} \cdot \int_0^t \underline{U}(t') dt'] \quad (C-22)$$

Using the assumed Gaussian distribution of the $b_{\underline{k}}$'s and the relation (C-3) we obtain

$$\langle B_{\underline{k}}(t) \rangle = B_{\underline{k}}(0) \exp[-D_3(\underline{k}, t)] \quad , \quad (C-23)$$

where

$$D_3(\underline{k}, t) = \int d^2 \underline{\ell} (\underline{k} \cdot \hat{\underline{\ell}})^2 [1 - \cos(\omega_{\underline{\ell}} t)] \Psi(\underline{\ell}) \quad . \quad (C-24)$$

For small t this becomes

$$D_3(\underline{k}, t) \approx \sigma^2 t^2 / 2 \quad , \quad \omega_{\underline{\ell}_0} t \ll 1 \quad , \quad (C-25)$$

where

$$\sigma^2 = \langle (\underline{k} \cdot \underline{U})^2 \rangle = \int d^2 \underline{\ell} (\underline{k} \cdot \hat{\underline{\ell}})^2 \omega_{\underline{\ell}}^2 \Psi(\underline{\ell}) \quad . \quad (C-26)$$

For $t \rightarrow \infty$, on the other hand, we have

$$D_3(\underline{k}, \infty) = \int d^2 \underline{\ell} (\underline{k} \cdot \hat{\underline{\ell}})^2 \Psi(\underline{\ell}) \quad . \quad (C-27)$$

We note that for the spectrum (C-4) the assumed condition (C-21) appears to be valid for the evaluation of D_3 .

When (C-25) is valid we may define an e-folding decay time as

$$T_d(3) = \sqrt{2} / \sigma \quad . \quad (C-28)$$

More generally, we may define the decay time with the relation

$$D_3(\underline{k}, T_d(3)) = 1 \quad . \quad (C-29)$$

This equation may, or may not, have a solution. When there is no solution, the advection mechanism is ineffective in destroying the "pattern". The single e-folding condition (C-29) is arbitrary and one may wish to define the decay time to correspond to several e-foldings.

A more systematic and formal description of the decay of (C-17) can be obtained using the method of Van Kampen (1974). To develop this we begin with the formulation of Watson and West (1975). Their equation of motion, when linearized in the pattern amplitudes $B_{\underline{k}}$, is of the form

$$\dot{B}_{\underline{k}} = T_2(B, b) + T_3(B, b) + \dots \quad (C-30)$$

Here T_2 and T_3 are quadratic and cubic, respectively in wave

amplitudes. If we ignore all but the T_2 term, (C-30) takes the form

$$\dot{B}_{\underline{k}}^{\underline{p}} = \sum_{\underline{l}} A_{\underline{k}}^{\underline{p}} B_{\underline{l}}^{\underline{p}} , \quad (C-31)$$

where

$$A_{\underline{k}}^{\underline{p}} = \sum_{\underline{l}} \delta_{\underline{k}-\underline{l}-\underline{p}} \{ 2\Gamma_{\underline{p}\underline{l}}^{\underline{k}} b_{\underline{l}}^{\underline{k}} \exp[i(\omega_{\underline{k}} - \omega_{\underline{p}} + \omega_{\underline{l}})t] \\ + \Gamma_{\underline{p}}^{\underline{k}-\underline{l}} b_{-\underline{l}}^* \exp[i(\omega_{\underline{k}} - \omega_{\underline{p}} - \omega_{\underline{l}})t] \} \quad (C-32)$$

The coefficients Γ are defined in Appendix A of Watson and West (1975).

The Van Kampen equation is

$$\frac{d}{dt} \langle B_{\underline{k}} \rangle = -K(t) \langle B_{\underline{k}} \rangle , \quad (C-33)$$

where

$$K(t) = - \int_0^t d\tau \langle A_{\underline{k}}^{\underline{p}}(t) A_{\underline{p}}^{\underline{k}}(t - \tau) \rangle . \quad (C-34)$$

Evaluation of this is straight forward, assuming that the $b_{\underline{l}}$ are Gaussian and the $\underline{l} \ll k, p$. The result is

$$K(t) = \int d^2 \underline{l} (\underline{k} \cdot \underline{\hat{l}})^2 \omega_{\underline{l}} \sin(\omega_{\underline{l}} t) \Psi(\underline{l}) \quad (C-35)$$

Integration of (C-33) leads to the expressions (C-23) and (C-24).

The three-wave interaction model (C-31) is the equivalent to the simple advection model described by (C-22). The fact that our decay function D_3 does not increase indefinitely with time reflects the lack of three-wave resonance. To find true decay to a vanishing pattern amplitude, we include the effects of T_3 in (C-30). This contains four-wave interactions. Higher order terms arising from T_2 also contribute four-wave interactions and must also be included.

Taking account of the four-wave interactions, we again have an equation of the form (C-31), but with the definition

$$A_{\underline{k}}^{\underline{p}} = \frac{1}{2} \sum_{\underline{l}, \underline{n}} \delta_{\underline{k} + \underline{n} - \underline{l} - \underline{p}} C_{\underline{p} \underline{l}}^{\underline{k} \underline{n}} b_{\underline{l}} b_{\underline{n}}^* \times \exp [i(\omega_{\underline{k}} - \omega_{\underline{p}} + \omega_{\underline{n}} - \omega_{\underline{l}})t] \quad (C-36)$$

The coefficients C here are defined in Appendix B of Watson and West (1975) [see specifically Eq. (47) of this reference]. Some rapidly oscillating terms have been dropped from (C-36). These terms do not contain frequency resonance and do not lead to a true pattern decay.

Evaluation of (C-34) using (C-36) now gives the decay rate

$$\begin{aligned}
 v(t) &= \text{Re } [K(t)] \\
 &= \frac{49}{128} \int d^2 \ell d^2 n \psi(\ell) \psi(n) \omega_\ell \omega_n [k \cdot (\ell + n)]^2 \\
 &\quad \times \frac{\sin(\beta t)}{\beta}
 \end{aligned} \tag{C-37}$$

where

$$\begin{aligned}
 \beta &= \omega_\ell - \omega_n + \omega_k - \omega_{|k+\ell-n|} \\
 &\approx \omega_\ell - \omega_n + \varepsilon(k) \cdot (n - \ell) \quad ,
 \end{aligned} \tag{C-38}$$

and

$$\varepsilon(k) = \nabla_k \cdot \omega_k \quad .$$

As $t \rightarrow \infty$, we obtain

$$v(\infty) = \frac{49\pi}{128} \int d^2\ell d^2n \Psi(\underline{\ell}) \Psi(\underline{n}) \omega_{\underline{\ell}} \omega_{\underline{n}} [\underline{k} \cdot (\underline{\ell} + \underline{n})]^2 \delta(\beta) \quad (C-39)$$

We see that asymptotically the four-wave resonance leads to a Langevin decay law of the form (C-19).

For finite times, we have the relation

$$\langle B_{\underline{k}}(t) \rangle = B_{\underline{k}}(0) \exp[-D_4(\underline{k}, t)] \quad , \quad (C-40)$$

where

$$\begin{aligned} D_4(\underline{k}, t) &= \int_0^t v(t') dt' \\ &= \frac{49}{128} \int d^2\ell d^2n \Psi(\underline{\ell}) \Psi(\underline{n}) \omega_{\underline{\ell}} \omega_{\underline{n}} [\underline{k} \cdot (\underline{\ell} + \underline{n})]^2 \\ &\quad \times [1 - \cos(\beta t)] / \beta^2 \end{aligned} \quad (C-41)$$

As $t \rightarrow \infty$, we obtain

$$D_4(\underline{k}, t) = v(\infty)t \quad . \quad (C-42)$$

To describe the implication of (C-25) and (C-41) we first

assume an isotropic ambient spectrum:

$$G(\theta) = 1 / (2\pi) \quad . \quad (C-43)$$

Although not realistic as a wind wave spectrum, (C-43) leads to reasonably accurate decay rate because of the integration over wave angles. A more realistic spectrum will be considered later.

Using (C-43) we can readily express (C-25) in form

$$D_3(k, t) = \left(\frac{\eta}{2} \right) \left(k / \ell_0 \right)^2 J_3(s) \quad ,$$

$$J_3(s) = \int_1^\infty [1 - \cos(\sqrt{x} s)] dx / x^3 \quad , \quad (C-44)$$

where

$$s \equiv \omega_{\ell_0} t \quad , \quad (C-45)$$

and we have replaced the exponential factor in (C-4) by a simple cut off at $\ell = \ell_0$. Similarly, we may evaluate (C-41) as

$$D_4(k, t) = \left(\frac{49}{96} \right) \left(k / \ell_0 \right)^2 J_4(s) \quad ,$$

$$J_4(s) = \frac{\pi}{2} + s^3 \int_0^\infty \frac{[1 - \cos u]}{(u + s)^3 u^2} du \quad . \quad (C-46)$$

In Figure C-3 we show the limiting decay (C-27) for three-wave interactions for several wavelengths $\lambda = 2\pi / k$ as functions of wind speed W . When $D_3(k, \infty)$ is small enough that the pattern cannot be considered destroyed, the three-wave mechanism is ineffective. We have arbitrarily chosen here

$$D_3(k, \infty) > 1 \quad (C-47)$$

as the condition of pattern destruction by three-wave interactions.

We now define a decay time T_d as

$$T_d = \text{smaller of } T_3, T_4 ,$$

$$D_3(k, T_3) = 1 ,$$

$$D_4(k, T_4) = 1 . \quad (C-48)$$

In Figure C-4 we show T_d as a function of wind speed for several wavelengths λ . The dashed lines represent an interpolation made from T_4 (upper region) to T_3 (lower region).

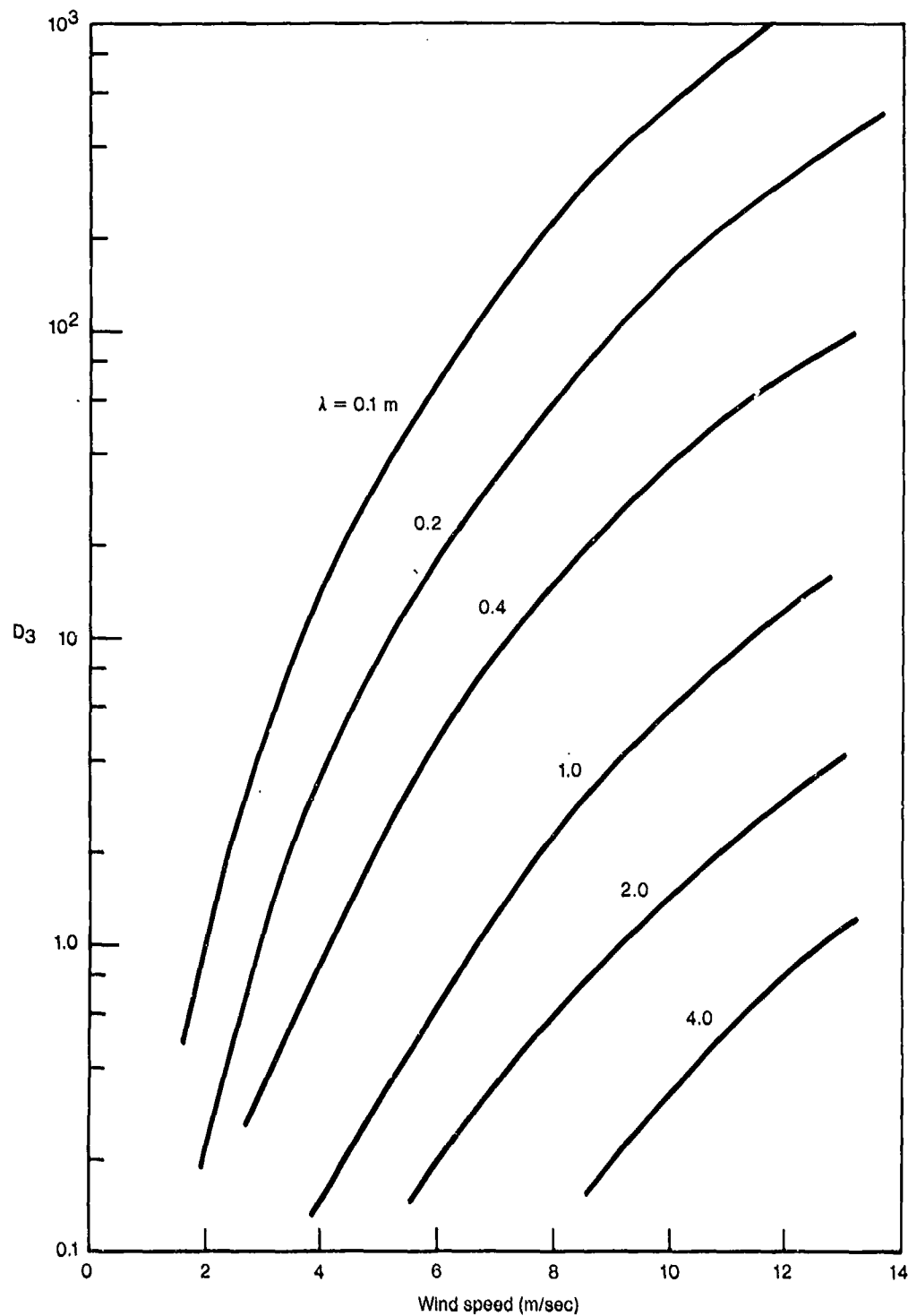


Figure C-3. The limiting decay function (4.13) due to three-wave interactions is shown as a function of wind speed for several wavelengths.

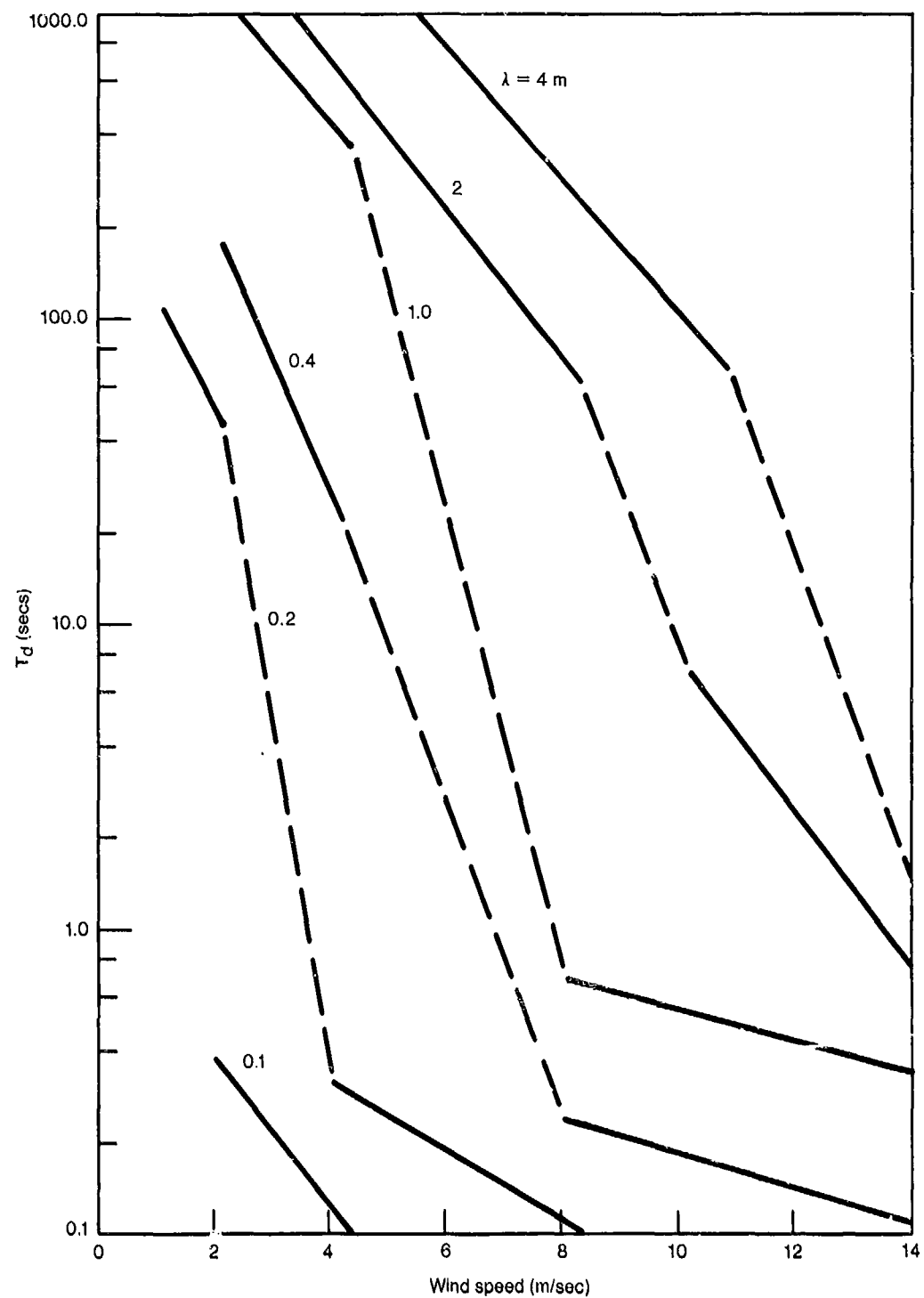


Figure C-4. The decay time (4.34) due to three- and four-wave interactions is shown.

A more realistic spectrum than (C-43) is that of Tyler et al. (1974):

$$F(\theta) = \cos^S(\theta) / L(S) ,$$

$$L(S) = 2 \sqrt{\pi} \Gamma \left(\frac{1}{2} S + \frac{1}{2} \right) / \Gamma \left(\frac{1}{2} S + 1 \right) , \quad (C-49)$$

where S is a function of k.

Using (C-49) we evaluate (C-26) as

$$\sigma^2 = n g(k^2 / k_o) [0.8 \cos^2 \alpha + 0.2 \sin^2 \alpha] ,$$

or

$$\sigma = 0.4 (W / \lambda) (\cos^2 \alpha + 0.25 \sin^2 \alpha)^{1/2} . \quad (C-50)$$

Here α is the angle of \underline{k} with respect to \underline{W} . Use of (C-43), on the other hand, would replace (C-50) by

$$\sigma = 0.3 (W / \lambda) .$$

The consequence of using the spectrum (C-49) does not seem very significant.

The decay time (C-28) obtained using the simple expression (C-50) is expected to be valid when

$$T_d < \frac{W}{g} \quad . \quad (C-51)$$

5. EVOLUTION OF THE PATTERN SPECTRUM

In this section we study the evolution of the pattern spectrum (C-7) due to the three wave mechanism. Using (C-22) we write

$$z_p(\underline{x}, t) = B_p(0) \exp[i(\underline{p} \cdot \underline{x} - \omega_p t - \underline{p} \cdot \underline{R})] \quad , \quad (C-52)$$

where

$$\begin{aligned} \underline{p} \cdot \underline{R} &= \underline{p} \cdot \int_0^t \underline{U} dt' \\ &= \sum_{\underline{\ell}} [(\underline{p} \cdot \hat{\underline{\ell}}) / 2] [b_{\underline{\ell}}^{\underline{\ell}} e^{i \underline{\ell} \cdot \underline{x}} (e^{-i \omega_{\underline{\ell}} t} - 1) + c.c.] \quad . \end{aligned} \quad (C-53)$$

In (C-52) we have assumed the initial pattern at $t = 0$ to be a plane wave of wavenumber \underline{p} . A more general pattern, representing a

superposition of plane waves, can readily be analyzed by the method presented in this section.

The wind velocity vector $\underline{W} = \hat{i}W$ is assumed to be directed parallel to the x-axis. The $b_{\underline{\ell}}'$'s are supposed to have a Gaussian distribution and the ambient spectrum is assumed to be described by (C-4). The expression (C-6) can be evaluated analytically. It is consistent with the condition (C-21) to assume that $r\ell \ll 1$, so we obtain

$$\begin{aligned} \Gamma_p(\underline{r}, t) = & \frac{1}{2} |B_p(0)|^2 \int d^2\ell \exp\{-i\underline{p} \cdot \underline{r}\} \exp\{-\int d^2\ell \Psi(\underline{\ell}) \\ & \times (\underline{r} \cdot \hat{\underline{\ell}})^2 (\underline{p} \cdot \underline{\ell})^2 [1 - \cos(\omega_{\underline{\ell}} t)] \} \end{aligned} \quad (C-54)$$

Equation (C-7) may also be evaluated analytically using the expression (C-54). The result gives the pattern spectrum as a function of time:

$$\begin{aligned} \Psi_p(\underline{k}, t) = & |B_p(0)|^2 / [8\pi \sqrt{c_1 c_2}] \\ & \times \exp\left[- (K_x \cos\phi - K_y \sin\phi)^2 / (4c_1) \right. \\ & \left. - (K_x \sin\phi + K_y \cos\phi)^2 / (4c_2) \right] \end{aligned} \quad (C-55)$$

Here

$$\underline{k} = \underline{k} - \underline{p} \quad ,$$

$$c_1 = \cos^2 \phi a_1 + \sin^2 \phi a_2 - 2 \sin \phi \cos \phi b$$

$$c_2 = \sin^2 \phi a_1 + \cos^2 \phi a_2 + 2 \sin \phi \cos \phi b$$

$$\tan 2\phi = 2b / (a_2 - a_1), \quad -\frac{\pi}{4} < \phi < \frac{\pi}{4} \quad ,$$

$$a_1 = \int d^2 \underline{\ell} \Psi(\underline{\ell}) (\hat{i} \cdot \hat{\ell})^2 (\underline{p} \cdot \underline{\ell})^2 [1 - \cos / \omega_{\ell} t] \quad]$$

$$a_2 = \int d^2 \underline{\ell} \Psi(\underline{\ell}) (\hat{j} \cdot \hat{\ell})^2 (\underline{p} \cdot \underline{\ell})^2 [1 - \cos(\omega_{\ell} t) \quad]$$

$$b = \int d^2 \underline{\ell} \Psi(\underline{\ell}) (\hat{i} \cdot \hat{\ell})(\hat{j} \cdot \hat{\ell})(\underline{p} \cdot \underline{\ell}) [1 - \cos(\omega_{\ell} t) \quad]$$

(C-56)

It is straightforward to evaluate these expressions for the spectral form (C-49). This is tedious and seems overly elaborate for our purpose. We therefore consider only the "peaked" spectrum corresponding to

$$G(\theta) = \delta(\theta)$$

(C-57)

and the isotropic spectrum (C-43).

For the peaked spectrum (C-57) we may simplify (C-55) to the form

$$\Psi_p(\underline{k}, t) = \frac{|B_p(0)|^2}{4\sqrt{\pi a_1}} \delta(k_y - p_y) \times \exp\left[-k_x^2 / (4a_1)\right] \quad (C-58)$$

In this case

$$a_1 = p_x^2 h \quad , \quad (C-59)$$

where

$$h = \eta \int \frac{d\ell}{\ell} \exp\left[-(\ell_0 / \ell)^2\right] [1 - \cos(\omega_\ell t)] \quad (C-60)$$

For the isotropic spectrum (C-23) we suffer no loss of generality in setting $p_y = 0$. Then

$$\Psi_p(\underline{k}, t) = \frac{|B_p(0)|^2}{8\pi\sqrt{a_1 a_2}} \exp\left[-(k_x - p_x)^2 / (4a_1)\right]$$

$$x \exp[-k_y^2 / (4a_2)] \quad . \quad (C-61)$$

Now,

$$a_1 = \frac{3}{8} p_x^2 h, \quad a_2 = \frac{1}{8} p_x^2 h, \quad b = 0 \quad (C-62)$$

where h is given by (C-60).

The integral (C-60) requires a cut-off at large ℓ and depends logarithmically on this cut-off. Thus, the scale separation condition (C-21) is not automatically satisfied by the spectrum (C-4), but must be imposed. For numerical evaluation we have done this by inserting a factor

$$[1 + (2\ell / p_x)^2]^{-1}$$

into the integrand in (C-60). In spite of this arbitrary imposition of a scale separation, our spectral evolution equations appear to be of some interest.

As was the case with the decay, as described by (C-27), the spectral spreading reaches an asymptotic limit for large t . To

illustrate our model, we consider the peaked model (C-58) for the case that $p_y = 0$. The spectrum is shown in Figure C-5 for $\lambda = 2\pi / p = 0.1$ m and $w = 1$ and 10 m/sec. In Figure C-6 we shown the spectrum for $\lambda = 0.4$ m and $w = 10$ and 20 m/sec. The spectrum described by (C-61) is similar, but evolves in both horizontal dimensions.

For these examples the asymptotic variance in the wavenumber is much less than the initial wavenumber of the wave train. Nevertheless, this spreading can decorrelate the wave phase coherence for a wavetrain of many wavelengths.

6. DIFFUSION IN WAVENUMBER SPACE

The four-wave interactions lead to an irreversible re-distribution of wave energy in wavenumber space. This is described by the term S_{nl} in (C-9). In the general case this is a very complex phenomena and beyond our present scope to discuss. For the case that the scale separation condition (C-21) can be assumed S_{nl} reduces to a simple diffusion mechanism

$$S_{nl} = \frac{\partial}{\partial k_i} D_{ij} \frac{\partial F_P}{\partial k_j} \quad (C-63)$$

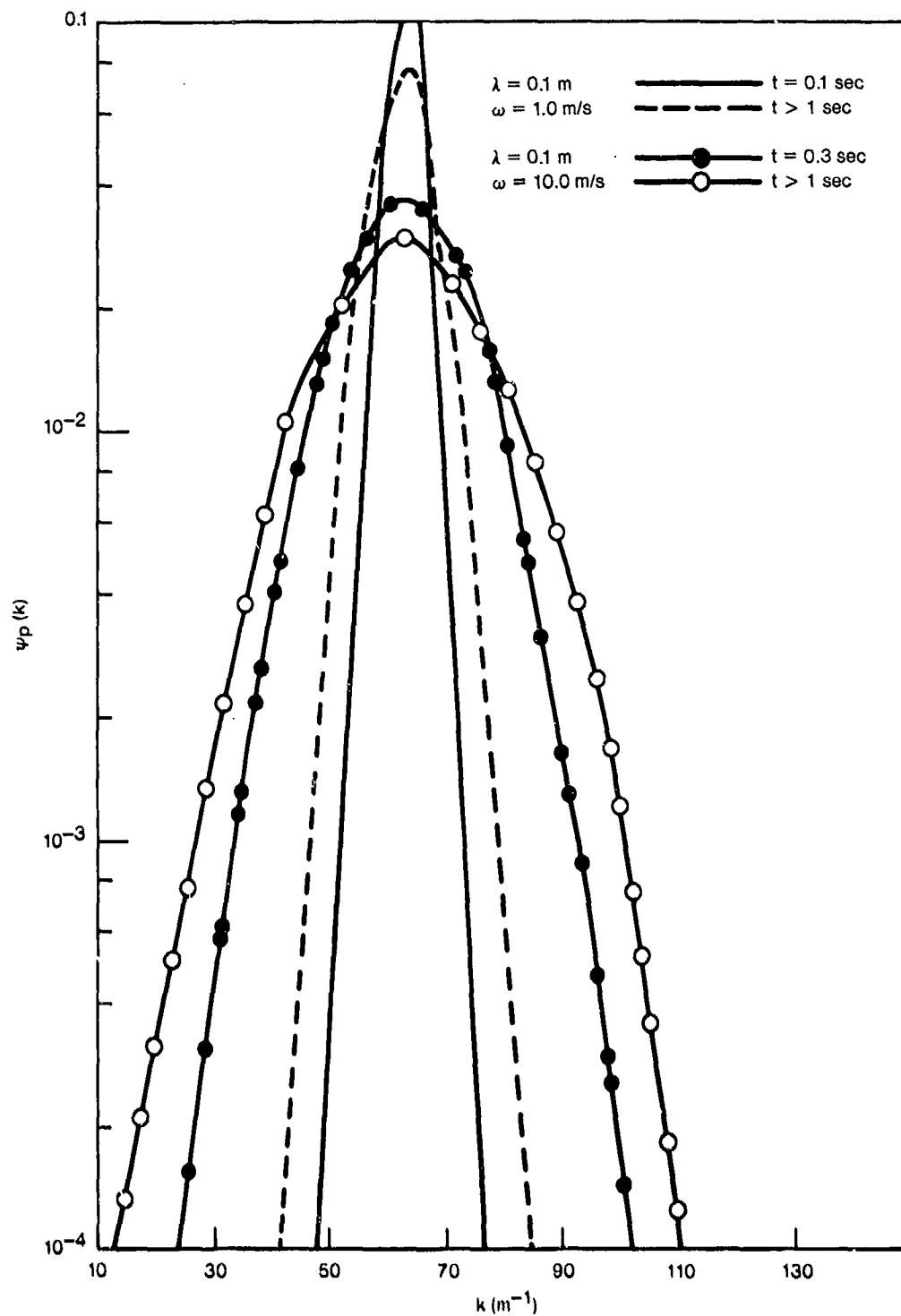


Figure C-5. The pattern spectral function (5.7), integrated over k_y , is shown for the case that $\lambda = 0.1$ m and $p_y = 0$. Wind speeds and times are indicated.

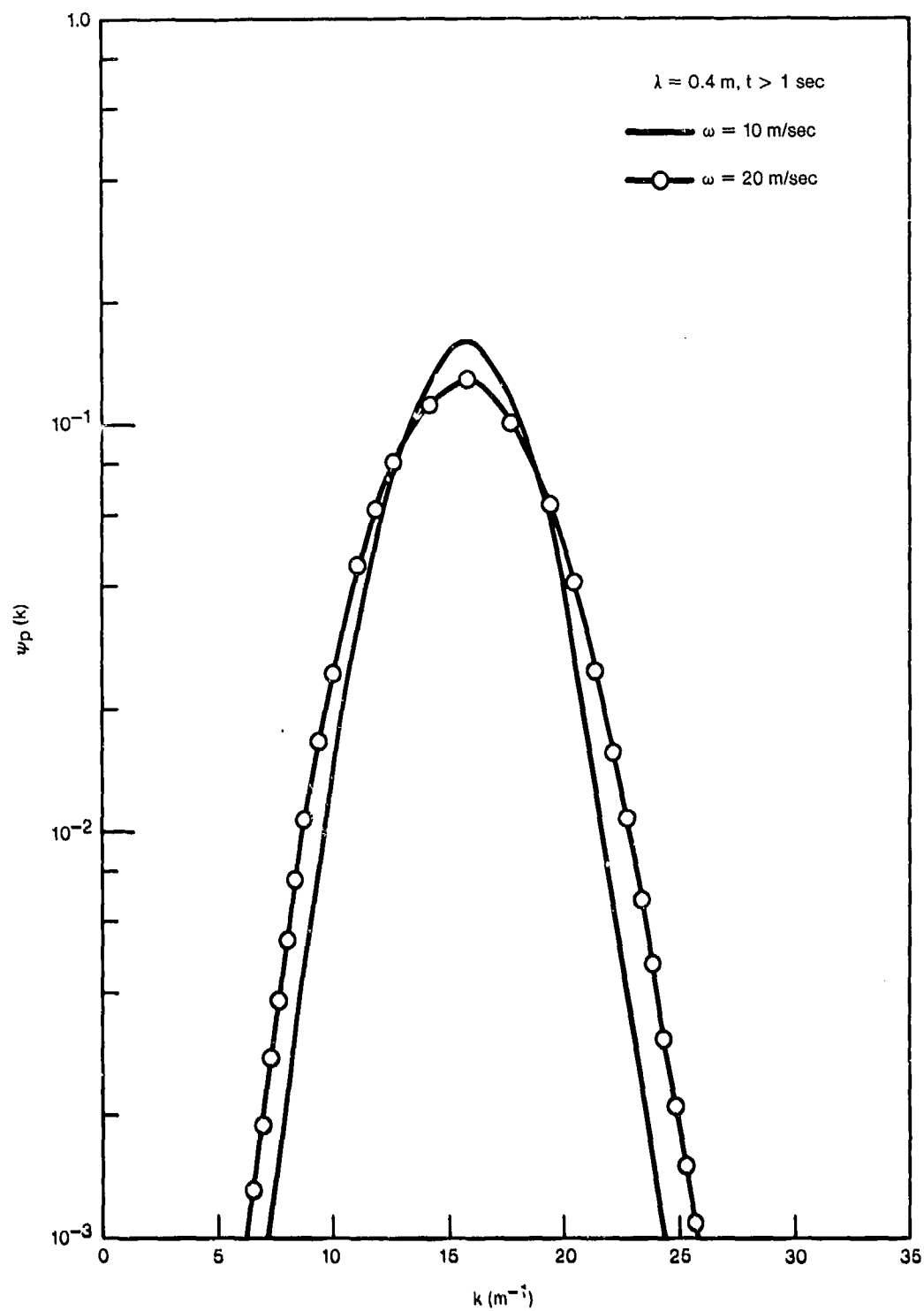


Figure C-6. The pattern spectral function for the conditions of Figure 5 is shown for case that $\lambda = 0.4 \text{ m}$.

Weak interaction theory leads to the expression

$$D_{ij} = \frac{1}{t} \left\langle \int_0^t \underline{k} \cdot \frac{\partial \underline{U}}{\partial \underline{x}_i} dt' \int_0^t \underline{k} \cdot \frac{\partial \underline{U}}{\partial \underline{x}_j} dt'' \right\rangle, \quad t \rightarrow \infty \quad (C-64)$$

Here \underline{U} is given by (C-20). For our application with the spectrum (C-4), the scale separation condition must be imposed by introducing a cut-off at wavenumber greater than some value, say ℓ_{may} . For this reason, only a brief qualitative discussion of (C-63) and (C-64) seems justified. A scalar diffusion coefficient,

$$D = \frac{1}{2} [D_{11} + D_{22}] ,$$

appears sufficient then, to characterize the diffusion. For the spectrum (C-49) we obtain

$$D \approx 3 \times 10^{-4} k^2 \omega_c, \quad \omega_c = \sqrt{g \ell_{\text{may}}} . \quad (C-65)$$

The variance Δk in an initial wave of wavenumber k is estimated at time t as

$$\begin{aligned} \Delta k &= \sqrt{Dt} \\ &= 2 \times 10^{-2} k \sqrt{\omega_c t} \end{aligned} \quad (C-66)$$

If we assume $\omega_c \sim 1 \text{ sec}^{-1}$ as reasonable, (C-66) implies times of the order of 10^3 seconds for significant pattern distortion. This is not incompatible with the four-wave time scales of Figure C-4.

7. CONCLUSIONS

We have seen that the decay of a wave pattern on the ocean surface is a complex phenomena. A number of mechanisms may contribute to this with many orders of magnitude variation in lifetimes, depending on pattern wavelengths and environmental conditions.

REFERENCES, APPENDIX C

Pierson, W.J. and L. Moskowitz, A proposed spectral form for fully developed wind seas based on the similarity theory of S.A. Kitaigorodskii, J. Geophys. Res., **69**, 5181-5190 (1964).

Wigner, E.P., On the quantum correction for thermodynamic equilibrium., Phys. Rev., **40**, 749-759 (1932).

Hasselmann, K., Nonlinear interactions treated by the methods of theoretical physics, Proc. Roy. Soc. London, **A299**, 77-100 (1967).

Phillips, O.M., The Dynamics of the Upper Ocean, 2nd edition, Cambridge University Press, Chapter 3 (1977).

Plant, W.J., A relationship between wind stress and wave slope, J. Geophys. Res., **87**, 1961-1967, (1982).

Garratt, J.R., Review of drag coefficients over oceans and continents, Mon. Weath. Rev., **105**, 915-922 (1977).

Van Kampen, N.G., Stochastic differential equations, Physica, **74**, 215-238 (1974).

Watson, K.M. and B.J. West, A transport-equation description of nonlinear ocean surface wave interactions, J. Fluid Mech., **70**, 815-826 (1975).

Tyler, G.L., C.C. Teague, R.H. Stewart, A.M. Peterson, W.H. Munk, and J.W. Joy, Wave directional spectra from synthetic aperture observations of radio scatter, Deep-Sea Research, **21**, 988-1016 (1974).

APPENDIX D

CORRECTIONS TO SAR ESTIMATES OF V-WAKE ANGLES

1.0 Introduction

Interpretation of synthetic aperture radar (SAR) images of ship wakes requires a detailed knowledge of some aspects of wake image shape. For example, the included angle of the wake allows one to argue kinematically that wake waves of a given wavelength are associated with the SAR signature of the wake because they have the appropriate group propagation velocity and were presumably generated near the ship. For the interior of the wake near the ship track a small change in wake geometry can change the physics one employs to explain the wake image. For example, a change from 2° to 3° in the angle θ , between wake and ship track, changes the associated wavelength by more than a factor two - from 20 cm to 45 cm. Hence rather complex corrections to SAR images may be necessary-- corrections which are not ordinarily made. During June 1984, Dr. David Lysenga and Mr. James Lyden of the Environmental Research Institute of Michigan (ERIM) described some of these corrections and

their applications to images collected during the Georgia Straits Experiment. Below we review these corrections and comment upon them.

2.0 Scanning Distortion

This correction refers to the finite time needed to collect the SAR image of a ship wake and the fact that the wake waves move during this time. If the aircraft flies parallel to the ship track, the correction can be substantial. It requires 8Js for a 200 kt aircraft to scan a 10 km wake image. During this time radar resonant (~30 cm) ocean waves travel some 56 m or about 6 SAR resolution cells. This would change the observed wake angle θ by about 0.2° . The effect is illustrated in Figure D-1 showing that the scanning distortion increases the observed θ for SAR movement opposite to the ship direction and vice-versa. The change in θ caused by this effect is $\theta_{\text{obs}} - \theta_{\text{true}} = \Delta\theta = -c_g/V$ where c_g is the group velocity of the wake waves associated with the SAR signature and V is the aircraft velocity taken positive when in the same direction as the ship velocity. Clearly scanning distortion is much less important for satellite SAR observations since $V \sim 7,000$ m/s and $\Delta\theta$ for ~30 cm waves becomes only $\sim 3 \times 10^{-3}$.

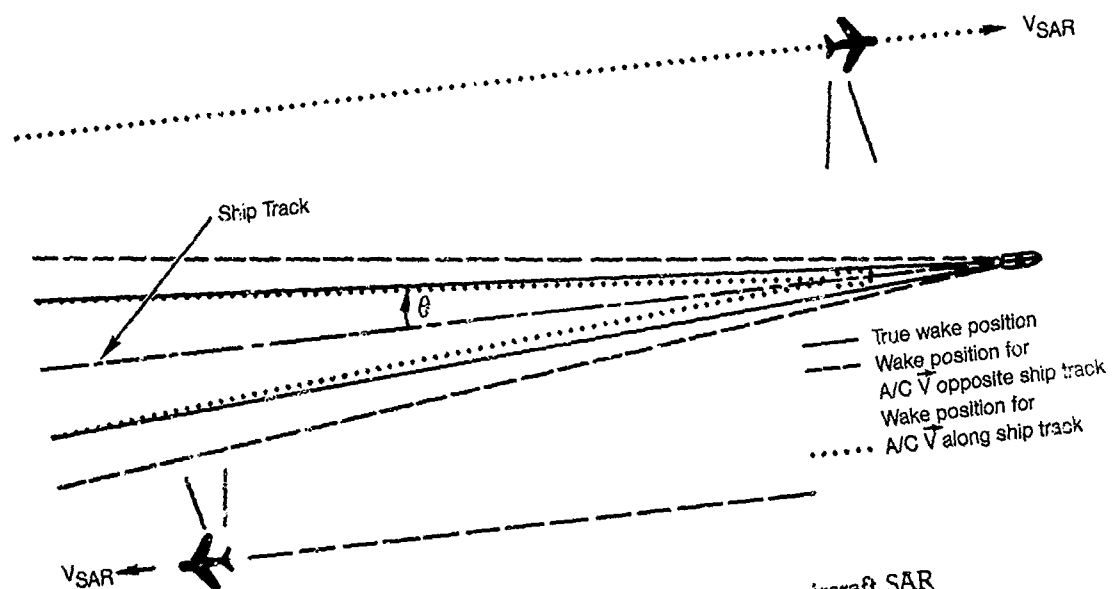


Figure D-1. Schematic illustration of scanning distortion for an aircraft SAR flying along or opposite a ship track. Typically the observed wake θ can be altered a few tenths of a degree due to this effect.

3.0 Doppler Shift

Since SAR uses the Doppler shift of the scatterers in a resolution cell to locate that resolution cell along the azimuth direction, any unexpected radial velocity (unrelated to the known movement of the SAR platform with respect to the ocean surface) can cause the resolution cell to be shifted along the azimuth direction by an amount $\Delta y = (R/V) V_r$ where R is the range to the resolution cell, V is the SAR velocity and V_r is the unexpected radial velocity. Bragg resonant waves of $\sim 30^\circ$ have a phase velocity of ~ 0.7 m/s and thus cause a typical displacement of $\Delta y \sim (100) 0.35 \sim 35$ m at an incidence angle of $\sim 30^\circ$. If a ship wake were all observed at a single angle of incidence, the wake arms would simply be shifted as a whole, the angle between the arms being unaffected. Here we neglect the velocity due to waves in the transverse wake since their velocity is primarily perpendicular to the radar ray path for ships traveling nearly along the SAR flight direction. However, different portions of the wake are observed at different incidence angles and therefore interact with different wavelength waves which in turn have different phase velocities and thus different Doppler displacements. Thus a small distortion of the wake angle is possible. Since Bragg resonant waves at larger incidence angles are shorter, they travel more slowly; yet they are

viewed more nearly along their velocity vector and have a larger component along the radar ray path. Since these two effects tend to cancel and wakes are most evident at small incidence angles and nearly parallel to the SAR velocity, this effect is usually a small distortion compared with the scanning distortion above. The distortion for satellite SAR is less than for aircraft SAR since the satellite SAR views the whole ship wake at very nearly the same angle of incidence.

4.0 Slant to Ground Range Conversion

The most primitive form of SAR image is the slant range image in which the image is displayed with true length along the SAR flight (y) direction but with the other dimension being range (R) along the radar ray path not along the Earth's surface. The conversion between slant and ground range is simply ground range $x = R \sin \theta'$ where R is slant range and θ' angle of incidence. Linear features which are straight lines in the ground range, (x,y) plane, are transformed into curved lines in the slant range (R,y) plane. This effect is illustrated in Figure D-2. For aircraft the distortion can be striking (especially at small θ' because θ' usually varies over a large range, e.g., 0° to 55° for the aircraft used in the Georgia Strait experiment. For spacecraft the

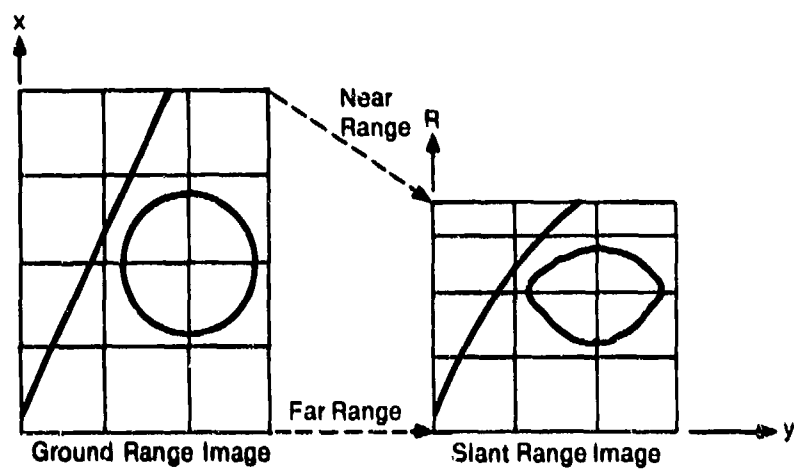
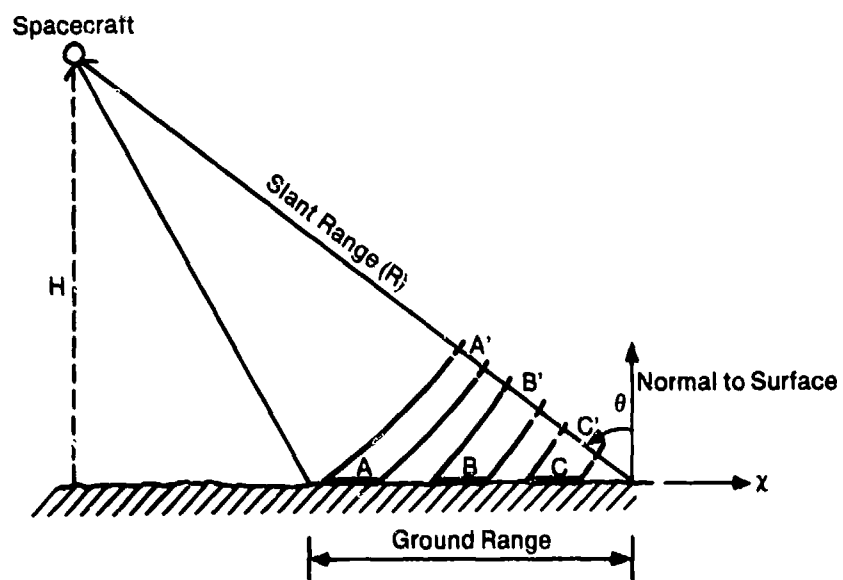


Figure D-2. Geometrical distortion in the slant-range imagery
(adapted from Fu and Holt, 1982).

effect is much less pronounced because only a small range of θ is used, e.g., 19° to 25° for SEASAT. Aircraft data are often presented in slant range images since they are more easily obtained. Satellite data on the other hand are nearly always provided in ground range coordinates. Obviously ground range images must be used to measure wake geometry.

The original measurement measurements of ship wake angles (θ) during the Georgia Straits (1983) experiment were made from slant range images and corrected approximately for the slant to ground range conversion. When measurements of θ on ground range images were made later, it was found that the original approximate correction used with slant range images--could be in error by about 0.7° . This effect coupled with the $\sim 0.2^\circ$ scanning error comprise the $\sim 1^\circ$ total correction overall.

5.0 Variation of Radar Cross Section with Angle of Incidence

The radar cross section σ^0 of an element of ocean surface is a function, not only of the local surface roughness, but also of the radar parameters and observational geometry. In particular σ^0 varies over some six orders of magnitude as angle of incidence varies from 0° to near 90° . So if the ship wake being observed runs

over a range of θ' , some distortion could be introduced because of the $\sigma(\theta')$ variation. That is, a linear wake feature would be shifted toward lower θ' since $d\sigma/d\theta$ is negative. The rate of change of σ with change in range is

$$d\sigma/dx = (d\sigma/d\theta')(d\theta'/dx) = (d\sigma/d\theta') R^{-1} \sec \theta'.$$
 For a typical aircraft $R \sim 10$ km and $d\sigma/d\theta' \sim 60$ dB/rad at maximum ($\theta' \sim 20^\circ$), $d\sigma/dx \sim 60 \times 10^{-4} \times 1.06 \sim 6 \times 10^{-3}$ dB/m. This is quite small, <0.1 dB for a one resolution cell displacement. So we conclude that this correction is negligible for aircraft and doubly so for spacecraft (where R is larger) provided θ' is not near 90° . For the SAR's of interest here θ is limited to $<60^\circ$.

6.0 Applications to Georgia Strait Experiment

From the discussion above it appears that the most important correction is to put the image in ground range coordinates. Next in importance is the scanning correction which may account for several tenths of a degree. The other corrections appear to be typically smaller. David Lyzenga & James Lyden of ERIM applied the aforementioned corrections to SAR images collected during the Georgia Straits Experiment. These corrections caused the arcs of the wake in pass 9-2 to meet some 400m ahead of the ship image as one would expect from Figure D-1. Corrections to narrow V wakes observed

during the Georgia Strait experiments resulted in wakes with half-opening angles of 2.5° which is near the angle expected if first-order Bragg resonant waves (~30 cm) are allowed to propagate from the ship track to the wake arm as observed by the SAR.

APPENDIX E

SPECULAR POINT SCATTERING FROM COHERENT WAVE PACKETS

1.0 Introduction

This and other reports (Zachariasen, et al., 1984; Hammond, et al., 1984, and Shuchman et al., 1983) describe SAR images of ship wakes. These reports and SAR data gathered during the Gulf of Alaska SAR - ship wake experiment have revealed a number of characteristics common to narrow angle wakes ($\theta \sim 2.5^\circ$ in Figure E-1). Some of these features are as follows:

1. Location: Wake arms are located at $\theta \sim 2.5^\circ$ which corresponds and kinetically to ~ 30 cm waves propagating outward from near the ship track.
2. Length: Wakes are very long extending in some cases more than 20 km behind the ship.
3. Fineness: The arms making up the bright wake are very fine, occupying a few SAR resolution cells or less.
4. Brightness: The bright arms making up the wake are indeed very bright, being like 6 to 24 dB above the surrounding background at ~ 1 km behind the ship.

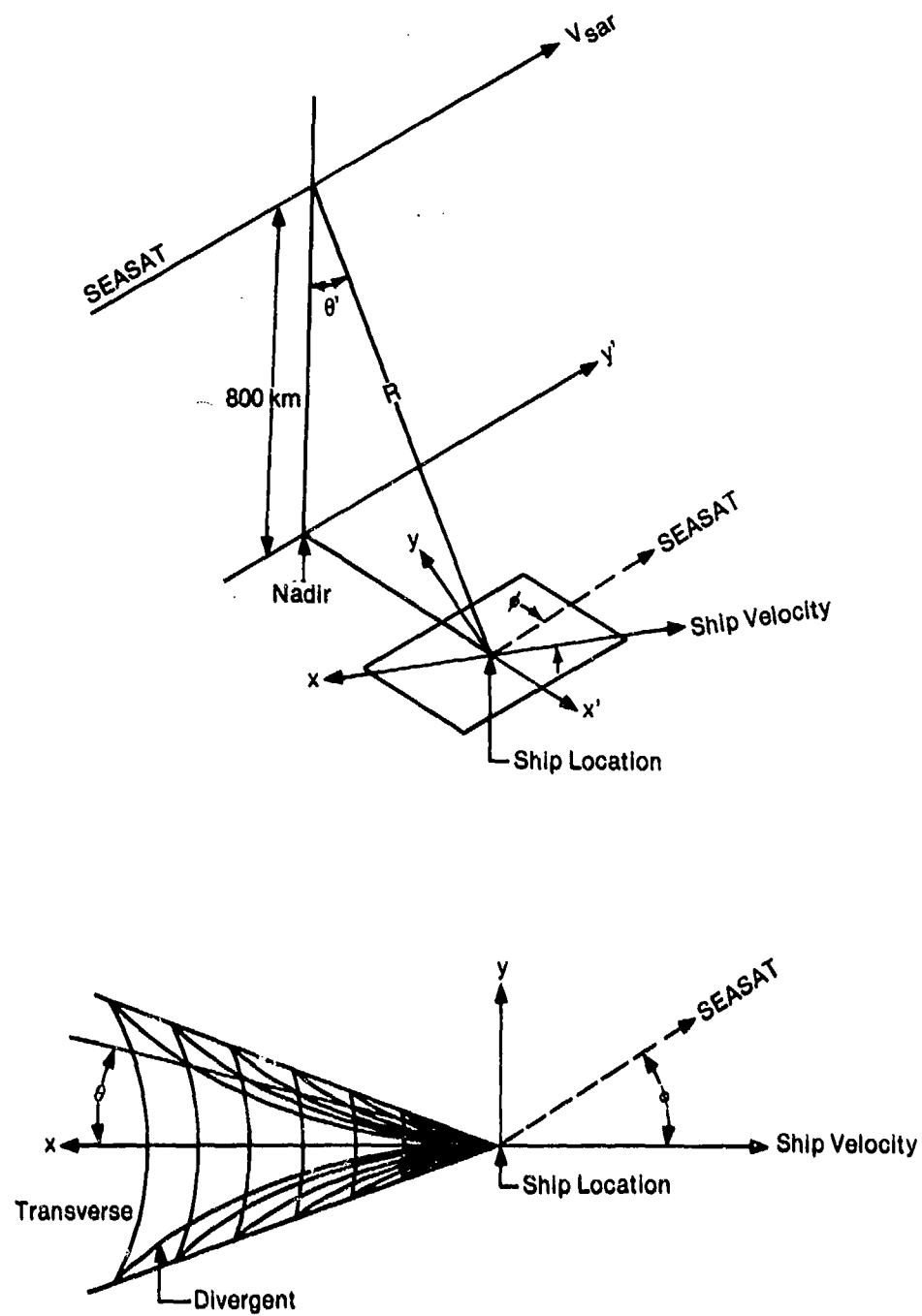


Figure E-1. Characteristics common to narrow angle wakes

5. Sensitivity to angle of incidence: Narrow wakes are very prominent at small incidence angles $\theta' \sim 20^\circ$, but have not been observed at high incidence angles $\theta' \sim 50^\circ$. Observation of the same ship on two successive SAR passes a few minutes apart at $\theta' \sim 25^\circ$ and $\theta' \sim 50^\circ$ is convincing evidence for this characteristic.
6. Disappearance in High Winds: Narrow angle, SAR ship wakes are most prominent at very low winds and are either very much reduced in length or disappear in high winds.

In this section we discuss an hypothesis for the scattering mechanism which addresses how the above characteristics of ship wakes occur in SAR images. The essence of the hypothesis is that the radar energy is backscattered from specular points located in small regions of coherent ~ 30 cm (or possibly ~ 60 cm) surface waves. These small regions are generated as part of the ship's surface (Kelvin) wake. Since the waves involved are short and of height \lesssim few centimeters, they are not particularly noticeable in a photograph of the wake. However, because microwave radar is sensitive to length scales of cm

to 10's of cm and particularly so to coherent patches of such waves, we suggest that these waves form the narrow vee SAR signature of a ship wake.

2.0 SPECULAR POINT SCATTERING FROM COHERENT WAVE PACKETS

2.1 Coherence of Wake Waves Within A Resolution Cell

One of the most striking visual features of a ship wake in calm water is the coherence of waves in the transverse and divergent portions of the wake. The divergent portion of the wake is of interest here since the SAR images of narrow wakes are for wake arms which are nearly parallel to the SAR velocity vector, i.e., θ and $\theta \sim$ a few degrees in Figure E-1. The cover photo of USS Quapaw (Hammond, et al., 1984) demonstrates this. Using the classical Kelvin wake analysis summarized by Dashen et al. (1982). We can calculate the variation in wave number between given angles $\theta = \theta_1$ and $\theta = \theta_2$ in Figure E-1. In Figure E-2 we show the variation in wavelength with θ over several ranges of θ .

The interesting point in Figure E-2b is that in the region of interest a SAR resolution cell contains a very small range of wavelengths! Within a typical 10m aircraft SAR resolution cell the

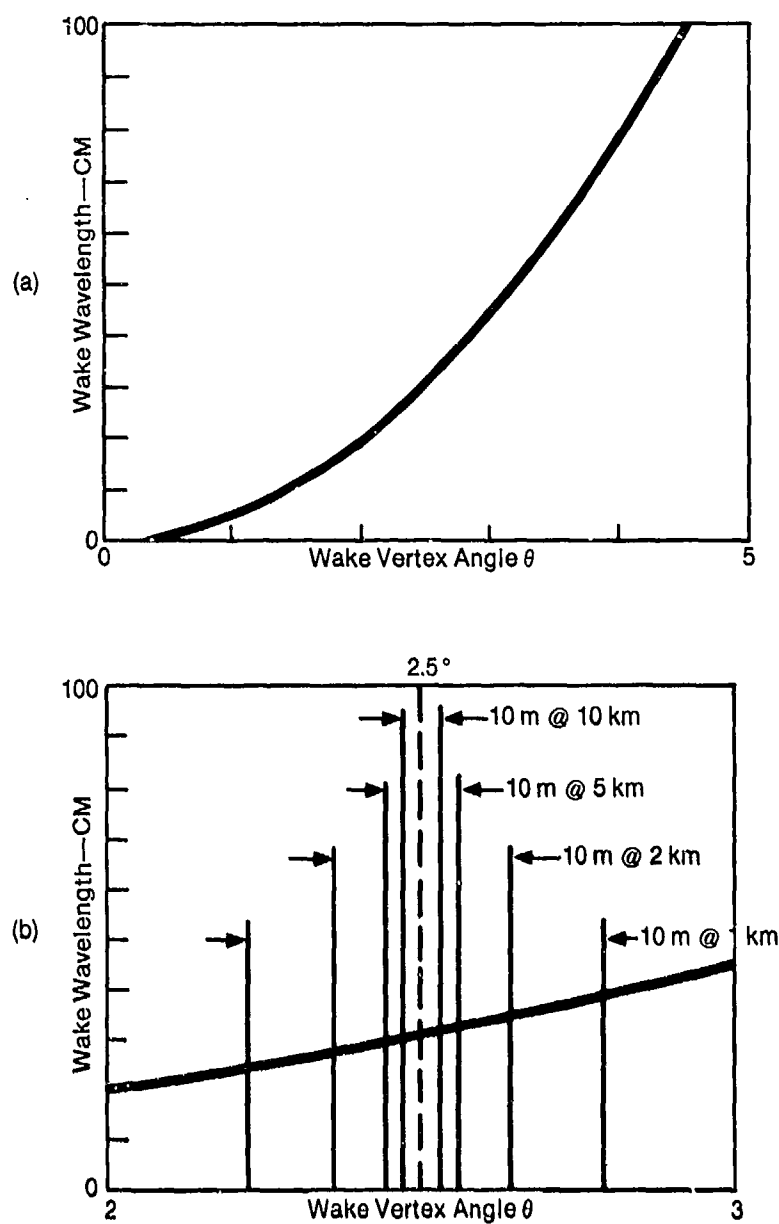


Figure E-2. Variation of classical Kelvin wavelength with angle θ (between ship track and line at angle to ship track - $\theta = \pm 19.4^\circ$ shows cusp lines of classical Kelvin wake). In (a) θ ranges from 0° to 5° . In (b) θ ranges from 2° to 3° and we show the range of angles and hence the range of wake wavelengths within a 10m SAR resolution cell at 1, 2, 5 and 10km distances behind the ship.

range of wavelengths (λ) around the 31 cm wavelength at the $\theta = 2.5^\circ$ point is ± 7 cm (0.23λ), ± 3.5 cm (0.11λ), ± 1.5 cm (0.05λ), and ± 0.75 cm (0.02λ) at distances of 1, 2, 5, and 10 km behind the ship (x in Figure E-1). The wavelength within a SAR resolution cell becomes more pure at greater distances behind the ship because the resolution cell subtends smaller and smaller variations of θ . Remember, of course, that these calculations refer to an ideal classical Kelvin wake in which the ship is a point source.

It is common to characterize the sea surface height fluctuations by a two-dimensional Fourier power spectrum (Phillips, 1977). Such a characterization assumes that the ocean surface waves are randomly phased as indeed they are for a wind roughened sea. In the case of ship wakes the waves are clearly not randomly phased in general, but rather coherent. Since the customary Fourier power spectrum throws away phase, it can not adequately characterize the waves in a ship wake. Other statistics which can characterize a partially coherent phenomena are necessary.

Perusal of the cover photo and Figure 19 of Hammond et al. (1984) quickly shows that for a real wake at $\theta \sim 2.5^\circ$ there are substantial deviations from the classical Kelvin wake picture.

First, the wake waves have a significant distribution in direction appearing to radiate from a sequence of compact sources spaced approximately at the wake's transverse wavelength. Thus the radius of curvature (in the horizontal plane) appears not to be that of the divergent portion of the classical Kelvin wake, but rather \sim the distance from the ship track to the point of interest. Second, the dominant wavelengths at a given location deviate from the classical Kelvin wake predictions of Figure E-2. Finally, the waves appear only partially coherent. The characteristics of wake waves at small θ suggested by Figure 19 are consistent with the intermittent source picture discussed in section 3 of this report.

Although this picture, suggested by observations, is somewhat different from the idealized classical Kelvin wake; features important for explaining the SAR signature of ship wakes are present. In fact some observational features of ship wake waves are necessary to explain the SAR observations. For example, the directional spread of $\sim 30^\circ$ is necessary to allow both arms of a narrow vee wake to be observed.

2.2 Radar Cross Section From Coherent Specular Scatterers

1. Definition of radar cross section

For people unfamiliar with radar, the notion of radar cross has some unexpected features when specular scattering is present.

The definition of radar cross section σ is given by

$$\sigma = \frac{\text{power reflected toward observer/unit solid angle}}{\text{incident power density}/4\pi}$$
$$= \lim_{R \rightarrow \infty} 4\pi R^2 \frac{|E_r|^2}{|E_i|^2} \quad (E-1)$$

where R is the distance between the radar and the scatterer, E_r is the reflected field strength at the observer and E_i is the incident field strength at the scatterer. The radar cross section is the area necessary to intercept the amount of incident power which, when scattered isotropically, produces the echo power actually observed. Thus σ is not a real cross sectional area, but rather a convenient hypothetical area. When σ is measured according to equation (E-1) it can be used in equation (E-2) to predict the backscatter power from a target, namely

$$P_r = \frac{P_t G_t A_e \sigma}{(4\pi)^2 R^4} \quad (E-2)$$

where P_r and P_t are the received and transmitted power, G_t is the transmitter antenna gain, A_e is the effective area of the receiver antenna, R is the range and σ the radar cross section (in units of area). When land or water surfaces are being observed the quantity σ^0 denotes the radar cross section σ of a unit area, i.e., $\sigma^0 = \sigma/A$ where σ is the cross section from area A .

2. Radar cross section of specular reflectors:

The counter intuitive property of σ^0 is that it can be and often is greater than unity. For example a lossless reflecting surface of area A oriented for specular reflection has a cross section of $\sigma \sim (4\pi A^2/\lambda^2)$. Note that σ is proportional to the physical area of the reflector squared because the scattering is coherent over the surface.

3. Kodis model for radar cross section of a sinusoidal corrugated surface

Kodis (1966) discusses the radar cross section from surfaces containing specular points. The theory is applicable to surfaces where the "physical optics" or "Kirchoff" method can be used, i.e., where $pk \cos^3 \theta \gg 1$ (E-3)

(Brehkovskikh, 1952). Such a surface is called "gently undulating."

Consider a sinusoidally corrugated surface of width W along the crest of a corrugation and length L perpendicular to the corrugation crests. The radar illuminates this corrugated surface in a direction perpendicular to the corrugation crests so that specular backscatter may arise. If the angle of incidence θ' is sufficiently small (near normal incidence) the the slope of the sinusoidal surface provides specular points. The radar cross section is then governed by the phasing of the specular points, i.e. for backscatter the radar cross section per unit width is (after Kodis)

$$\sigma \approx (\pi \rho_s / \lambda) \left[N + 2 \sum_{m=1}^{n-1} (N - m) \cos m \phi \right] \quad (E-4)$$

where ρ_s is the radius of curvature of the sinusoidal surface at the specular point, λ is the radar wavelength, N the number of specular point illuminated and $\phi = 2 k \lambda n_x$ where k is the radar wavenumber, λ the sinusoidal surface wavelength and n_x is the component of the surface normal along the illumination or x -direction. As with a grating, backscatter maximum occur when ϕ is an integral multiple of 2π leading to a Bragg condition

$$\lambda n_x = p \lambda / 2, \quad p = 1, 2, \dots \quad (E-5)$$

When the Bragg condition is fulfilled, the radar cross section for backscatter from an area of length L and width W becomes a maximum, namely (after Kodis)

$$\sigma_{\max} \approx (2\pi\rho_s/\lambda) N^2 (LW) \quad (E-6)$$

where N is the number of specular points illuminated.

For a randomly rough surface fulfilling (3) Kodis obtains a backscatter cross section of

$$\sigma \sim \pi \overline{R_a R_b} \langle N \rangle \quad (E-7)$$

where R_a and R_b are the principle radii of curvature of a specular point and $\langle N \rangle$ is the mean number of specular points in the illuminated region. σ becomes σ^0 if we take $\langle N \rangle$ to be the mean number of specular points per unit area. The important point to note here is that σ goes as N^2 for the coherent corrugated surface, but as N for the randomly rough surface.

2.3 Radar Cross Section for a SAR Resolution Cell Containing Coherent Specular Scatterers

We now apply the notions above to a SAR resolution cell containing at least some portion which is filled with coherent waves as discussed above. We consider sinusoidal waves in some detail and discuss other wave shapes briefly.

1. Sinusoidal Waves.

Kodis (1966) Consider a sinusoidal corrugated surface of the form

$$\zeta(x) = h \sin (2\pi x/\ell) \quad (\text{E-8})$$

where $-(L/2) \leq x \leq (L/2)$. The maximum slope of the surface is $(2\pi h/\ell)$ so that specular points will appear only for angles of incidence θ' smaller than

$$\tan \theta' = 2\pi h/\ell . \quad (\text{E-9})$$

The radius of curvature at the specular points is

$$\rho_g = \ell^2 / (4\pi h \cos^2 \theta' \sin \psi) \quad (\text{E-10})$$

where $\cos \psi = (\ell/2\pi h) \tan \theta'$. In general there are two specular points such that $(2\pi/\ell) x_{s1} = \psi$ and $(2\pi/\ell) x_{s2} = 2\pi - \psi$. The cross section of equation (E-6) assumes that only one of the two is illuminated, i.e., one is shadowed or the two coincide at the point of maximum slope.

As a specific case, we take $\theta' = 23^\circ$ as with SEASAT and $\lambda = 23$ cm for an L-band SAR yielding a Bragg resonant ℓ of ~ 30 cm. In Table E-1 we note the minimum wave amplitude (h_s) required to produce a specular point at the point of maximum slope on the wave. Also shown is the maximum slope for the required h_s and $\ell \sim 30$ cm. Since waves tend to break when they have maximum slopes above ~ 0.5 , it is clear that for sinusoidal waves, angles of incidence θ' above about 30° will not produce specular points and thus no radar backscatter via this mechanism. We also show ρ_s^* for conditions such that $\psi = 180^\circ \pm 150^\circ$, i.e., near but not at the point of maximum slope ($\psi = 0^\circ$). If the specular points are precisely at the point of maximum slope, then $\sin \psi = 0$ and ρ_s becomes infinitely large.

In a 10×10 m resolution cell with $\rho_s \sim 0.9$ m, and $\lambda \sim 0.23$ m we have from equation (E-6) and $\sigma^0 = \sigma/\text{Area}$

TABLE E-1
SINUSOIDAL WAVE PARAMETERS

θ	h_s -cm	MAXIMUM SLOPE	p_s^* -cm
5	0.42	0.09	343
10	0.84	0.16	176
20	1.74	0.36	93
30	2.76	0.58	69
40	4.01	0.84	61
50	5.69	1.19	61
60	8.27	2.11	69

$$\sigma_{\max}^o \sim 25 N^2 \quad (\text{E-11})$$

where N is the number of coherent specular points matching the Bragg condition (equation (E-5)). Referring to Figure E-3 we see that even a few coherent corrugations will produce a normalized radar cross section σ^o which is greater than the observed radar cross section of the ocean by at least 10 dB.

Now equation (E-6) refers to a straight corrugation stretching clear across the resolution cell. As we noted above, the observed ~ 30 cm waves, have significant curvature in the horizontal plane and clearly do not have wave crests 10 m long. Further, one might ask, is the illumination coherent over the resolution cell? Zachariassen et al. (1983) note that for all common SAR systems the Fresnel zone size is larger than the resolution cell size. If we accept the idea that the ~ 30 cm waves are generated by an intermittent source near the ship track, then the radius of curvature in the horizontal plane must be about the distance from the ship track to the wake's a SAR signature at $\theta \sim 2.5^\circ$ i.e. $R_h \sim 0.04x$ or $R_h \sim 44$ m at one kilometer behind the ship. The coherent length of wave crest is $l_c \sim \sqrt{\lambda R_h/2}$ or if $\lambda \sim 0.23$ m and $R_h \sim 44$ m, $l_c \sim 2.2$ m. Thus the σ^o from equation (E-11) should

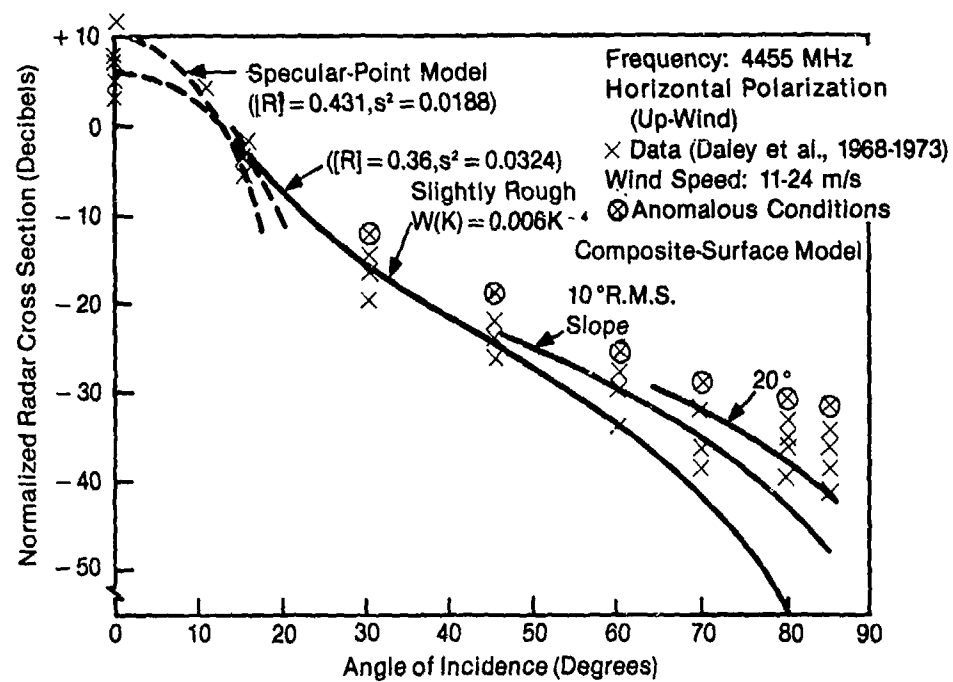


Figure E-3. Observations and models of the ocean's normalized radar cross section as a function of angle of incidence θ' . Although this plot is for C-band (~ 4.5 GHz), it differs little from L-band (1.2 GHz). After Valenzuela (1978).

be lowered at least by the factor (λ_c/W) where W is the resolution cell width. Thus equation (2.11) becomes:

$$\sigma_{\max}^0 \sim 5.5 N^2 \quad (\text{E-12})$$

which is still more than 10 dB above the level of Figure E-3.

In summary the point of this computation is to show that even a small patch of several coherent waves with specular points can provide a radar cross section significantly above that of the average ocean.

2. Cynoidal, Cusped and Breaking Waves.

Realistic surface waves can have cynoidal or cusped shapes. These shapes have regions with radii of curvature smaller than the radar wavelength and thus can be modeled approximately as scattering wedges. Some work on wedge scattering in connection with the ocean has been done by Lyzenga et al (1983) and a laboratory wave tank by Lake and Kwok at TRW. Waves of ~ 30 cm lengths with these shapes could also produce specular scattering from coherent wave packets either via specular points or by wedge shaped crests. The radar cross section from these shapes would clearly differ from

equations (E-11 or E-12), but if the waves were in coherent sets the total cross section would go as N^2 rather than N . Hence sets of coherent wedge scatters could produce σ^0 significantly above that of the average ocean.

3. Importance of Polarization

Nearly all SAR's observing the ocean, such as SEASAT and the NASA L-band aircraft SAR, use HH polarization. Thus horizontally polarized (E field perpendicular to the plane of incidence) waves are transmitted and received. Since the coherent waves discussed in this section have much longer coherence lengths in the horizontal direction, one would expect a stronger wake signature in HH as opposed to VV polarization. This effect would be particularly striking if wedge like structures were present. So SAR images of ship wakes simultaneously in both HH and VV (and possibly HV or VH polarization) would carry important information regarding the wave structures responsible for the observed scattering.

2.4 Validity of Coherent Specular Model

The key question concerning the validity of the hypothesis suggested here is what are the wake waves responsible for the SAR signature really like? Do they satisfy the curvature condition

equation (E-3)? Do they contain specular points? Are wedge-like structures involved? How coherent are the real waves in nature? This coherent specular hypothesis rests on the conjecture that real wake waves at ~ 30 cm length are enough like an ideal coherent-sinusoidally-corrugated surface that a large radar cross section is produced.

3.0 APPLICATION TO SAR WAKE FEATURES

Below we discuss one by one the observed features of ship wakes observed by L-band SAR. In each case we show how this coherent-specular-scatter hypothesis can explain or help explain the observed signature. Since the scattering surface is not well characterized, these arguments are at best semi-quantitative.

3.1 Location of Wake

SAR images at L-band find bright wake signatures at $\theta \sim 2.5^\circ$ (Figure E-1). This value of θ corresponds to the time required for ~ 30 cm waves to propagate from the ship track to $\theta \sim 2.5^\circ$. Thus one can argue kinematically that short gravity waves which fulfill the Bragg resonance condition of equation (E-5) are present at the proper location. Hammond et al. (1984) find from

photographic data that the wave energy present at $\theta \sim 2.5^\circ$ is concentrated more at wavelengths of from 50 to 90 cm than from 10 to 50 cm. This results is, not comprehensive, however, being composed of one observation. Nevertheless 60 cm waves also fulfill the Bragg condition of equation (E-5). They would produce a lower (but still large) cross section because N would be smaller in equations (E-11) and (E-12).

3.2 Length of Wake

SAR images of ship wakes stretch to 20 km or more along the x-direction in Figure E-1. Given that 30 cm waves decay with an e-folding time considerably less than the ~ 30 min required to generate such a long wake. One suspects that there must be some mechanism which enhances the radar cross section to at least partially counteract the wave decay. The coherent specular hypothesis provides such a mechanism. In Figure E-2 we showed how the spread in wavelength of classical Kelvin wake waves within a SAR resolution cell becomes smaller as the resolution cell in question was located further behind the ship. Thus as x increases and ~ 30 cm waves decay, the purity of the wavelength within a 10×10 m resolution cell increases. Hence the fraction of the resolution cell covered by a resonant corrugated surface would increase, N would increase

and σ would increase according to equation (E-6). However, as ~ 30 cm waves decay, they become less able to fulfill equation (E-9) and thus produce specular points for a given angle of incidence θ' .

3.3 Fine (Narrow) Wake Features

The fact that SAR ship wake features occur only one to a few SAR resolution cells suggests that a sharp resonance phenomena is present. The coherent specular hypothesis fits this observational fact since the Bragg condition (equation (E-5)) must be fulfilled in order to obtain the maximum cross section of equation (E-6). Scattering via the slightly rough Bragg resonant mechanism (Valenzuela, 1979) also fits well with the fineness of the linear wake features. The coherent specular mechanism differs from the slightly rough mechanism in that the former depends on specular scattering from coherently phased waves while the later does not depend on specular scattering. An analysis of the slightly rough Bragg mechanism needs to be done to compare it with the hypothesis pursued here. However, such a comparison is beyond the scope of this report.

3.4 Strong Wake Signature

The observation that SAR wake signature in calm water are very strong (~ 8 to 18 dB above the background) suggests that a strong scattering mechanism is required. In section 2 above we showed how even a small N in equation (E-12) could provide a radar cross section some 10 to 20 dB above the normal ocean cross section of Figure E-3. In F below we discuss why such a large enhancement in σ is not seen when the wind rises and other waves beside wake generated waves are present.

3.5 Disappearance of Narrow Vee SAR Wakes at High Incidence Angles

During the Gulf of Alaska SAR ship wake experiment the same ship was observed at $\sigma' \sim 50^\circ$ the same ship in the same background produced no wake in the L-band SAR image. The coherent specular hypothesis explains this qualitatively in Table E-1. At large σ' large wave slopes are required to produce specular points. For $\sigma' \gtrsim 30^\circ$ the Bragg resonant waves break before they can produce the large required slopes. Further, as σ' increases the Bragg resonance condition requires shorter surface waves for resonance. At $\sigma' = 50^\circ$ the first order resonance is at 15 cm rather than 30 cm. The shorter waves decay faster and may be generated at less

strength and less coherently by the ship - more reasons why narrow SAR wakes are not observed at large σ .

3.6 Disappearance of Narrow Wakes as Wind Speed Increases

If coherent specular scattering can produce such a large σ on a calm surface, why can't this mechanism make narrow wakes visible in even high sea states. We argue that as the wind increases not only does the background σ (surrounding the location of the narrow vee wake) rise but also that the wind generated waves destroy the coherence of the wake related waves. It is easy to visualize how wind generated waves would both rougher the specular points (reducing their effectiveness) and move the coherent corrugations around making them incoherent.

REFERENCES, APPENDIX E

Hammond, R.R., R.R. Buntzen and E.E. Floren, "Use of Ship Wake Patterns in the Evaluation of SAR Ocean Wave Imaging Mechanisms," Interim Report, Naval Ocean System Center, San Diego, CA 92152 (1984).

Shuchman, R.A., E.S. Kasischke, D.R. Lyzenga and A. Klooster, Jr., "SAR Ship Wake Signatures," ERIM Topic Report 157700-1-X, Environmental Research Institute of Michigan, Ann Arbor, MI 48107 (1983).

Zachariasen, F., SEASAT II JSR-83-203, The MITRE Corporation McLean, VA 22102 (1983).

Dashen, R., W. Munk, and F. Zachariasen, "Letter to Andreassen and Harpen," JSN-83-01, The MITRE Corporation, McLean, VA 22102 (1982).

Phillips, O.M., The Dynamics of the Upper Ocean (2nd edition), Cambridge University Press, Cambridge, U.K. (1977).

Kodis, R.D., A note on the theory of scattering from an irregular surface, IEEE Trans. Antennas and Propagation, AP-14, 77-82 (1966).

Brekhovskikh, L.M., The diffraction of waves by a rough surface, Zh. Eksper. i Teor. Fiz., 23, 275-289 (1952).

Valenzuela, G.R., Theories for the interaction of electromagnetic and ocean waves - review, Boundary Layer Meteorology, 13, 61-85 (1978).

Lyzenga, D.R., A.L. Maffett and R.A. Shuchman, The contribution of wedge scattering to the radar cross section of the ocean surface, IEEE Trans. Geoscience and Remote Sensing, GE-21, 502-505 (1983).

Distribution List

Dr. Marv Atkins
Deputy Director, Science & Tech.
Defense Nuclear Agency
Washington, D.C. 20305

National Security Agency
Attn RS: Dr. N. Addison Ball
Ft. George G. Meade, MD 20755

Mr. Anthony Battista [3]
House Armed Services Committee
2120 Rayburn Building
Washington, D.C. 20515

Mr. Steve Borchardt
Dynamics Technology
Suite 200
22939 Hawthorne Boulevard
Torrance, CA 90505

Mr. Rod Buntzen
NOSC
Code 1603B
San Diego, CA 92152

Dr. Curtis G. Callan, Jr.
Department of Physics
Princeton University
Princeton, NJ 08540

Mr. Gerald Cann
Principal Assistant Secretary
of the Navy (RES&S)
The Pentagon, Room 4E736
Washington, D.C. 20350

Dr. Kenneth M. Case
The Rockefeller University
New York, New York 10021

Dr. Robert Cooper [2]
Director, DARPA
1400 Wilson Boulevard
Arlington, VA 22209

Dr. Roger F. Dashen
Institute for
Advanced Study
Princeton, NJ 08540

Dr. Russ E. Davis
Scripps Institution
of Oceanography
(A-030), 301 NORPAX, UCSD
La Jolla, CA 92093

Defense Technical Information [2]
Center
Cameron Station
Alexandria, VA 22314

The Honorable Richard DeLauer
Under Secretary of Defense (R&E)
Office of the Secretary of
Defense
The Pentagon, Room 3E1006
Washington, D.C. 20301

Director [2]
National Security Agency
Fort Meade, MD 20755
ATTN: Mr. Richard Foss, A05

CAPT Craig E. Dorman
Department of the Navy, OP-095T
The Pentagon, Room 5D576
Washington, D.C. 20350

CDR Timothy Dugan
NFOIO Detachment, Suitland
4301 Suitland Road
Washington, D.C. 20390

Dr. Frank Fernandez
ARETE Assoc.
P.O. Box 350
Encino, CA 91316

Distribution List

Mr. Richard Gasparouic
APL
Johns Hopkins University
Laurel, MD 20707

Dr. Larry Gershwin
NIO for Strategic Programs
P.O. Box 1925
Washington, D.C. 20505

Dr. S. William Gouse, W300
Vice President and General
Manager
The MITRE Corporation
1820 Dolley Madison Blvd.
McLean, VA 22102

Dr. Edward Harper [10]
SSBN, Security Director
OP-021T
The Pentagon, Room 4D534
Washington, D.C. 20350

Mr. R. Evan Hineman
Deputy Director for Science
& Technology
P.O. Box 1925
Washington, D.C. 20505

Dr. Richard Hoglund
Operations Research Inc.
Room 428
1400 Spring Street
Silver Spring, MD 20910

Mr. Ben Hunter [2]
CIA/DDS&T
P.O. Box 1925
Washington, D.C. 20505

The MITRE Corporation [25]
1820 Dolley Madison Blvd.
McLean, VA 22102
ATTN: JASON Library, W002

Mr. Jack Kalish
Deputy Program Manager
The Pentagon
Washington, D.C. 20301

Mr. John F. Kaufmann
Dep. Dir. for Program Analysis
Office of Energy Research, ER-31
Room F326
U.S. Department of Energy
Washington, D.C. 20545

Dr. George A. Keyworth
Director
Office of Science & Tech. Policy
Old Executive Office Building
17th & Pennsylvania, N.W.
Washington, D.C. 20500

Mr. Jerry King [3]
RDA
P.O. Box 9695
Marina del Rey, CA 90291

MAJ GEN Donald L. Lamberson
Assistant Deputy Chief of Staff
(RD&A) HQ USAF/RD
Washington, D.C. 20330

Dr. Donald M. LeVine, W385 [3]
The MITRE Corporation
1820 Dolley Madison Blvd.
McLean, VA 22102

Mr. V. Larry Lynn
Deputy Director, DARPA
1400 Wilson Boulevard
Arlington, VA 22209

Distribution List

Dr. Joseph Mangano [2]
DARPA/DEO
9th floor, Directed Energy Office
1400 Wilson Boulevard
Arlington, VA 22209

Mr. Walt McCandless
4608 Willet Drive
Annandale, VA 22003

Mr. John McMahon
Dep. Dir. Gen. Intelligence
P.O. Box 1925
Washington, D.C. 20505

Director
National Security Agency
Fort Meade, MD 20755
ATTN: William Mehuron, DDR

Dr. Marvin Moss
Technical Director
Office of Naval Research
800 N. Quincy Street
Arlington, VA 22217

Dr. Walter H. Munk
9530 La Jolla Shores Drive
La Jolla, CA 92037

Dr. Julian Nall [2]
P.O. Box 1925
Washington, D.C. 20505

Director
National Security Agency
Fort Meade, MD 20755
ATTN: Mr. Edward P. Neuburg
DDR-FANX 3

Prof. William A. Nierenberg
Scripps Institution of
Oceanography
University of California, S.D.
La Jolla, CA 92093

Dr. John Penhune
Science Applications, Inc.
MS-8
1200 Prospect Street
La Jolla, CA 92038

Mr. Alan J. Roberts
Vice President & General Manager
Washington C³ Operations
The MITRE Corporation
1820 Dolley Madison Boulevard
Box 208
McLean, VA 22102

Los Alamos Scientific Laboratory
ATTN: C. Paul Robinson
P.O. Box 1000
Los Alamos, NM 87545

Mr. Richard Ross [2]
P.O. Box 1925
Washington, D.C. 20505

Mr. Richard Ruffine
OUSDRE
Offensive & Space Systems
The Pentagon, Room 3E129
Washington, D.C. 20301

Dr. Phil Selwyn
Technical Director
Office of Naval Technology
800 N. Quincy Street
Arlington, VA 22217

Dr. Eugene Sevin [2]
Defense Nuclear Agency
Washington, D.C. 20305

Mr. Omar Shemdin
JPL
Mail Stop 183501
4800 Oak Grove Drive
Pasadena, CA 91109

Distribution List

Mr. Robert Shuckman
P.O. Box 8618
Ann Arbor, MI 48107

Dr. Joel A. Snow [2]
Senior Technical Advisor
Office of Energy Research
U.S. DOE, M.S. E084
Washington, D.C. 20585

Mr. Alexander J. Tachmindji
Senior Vice President & General
Manager
The MITRE Corporation
P.O. Box 208
Bedford, MA 01730

Dr. Vigdor Teplitz
ACDA
320 21st Street, N.W.
Room 4484
Washington, D.C. 20451

Mr. Anthony J. Tether
DARPA/STO
1400 Wilson Boulevard
Arlington, VA 22209

Dr. Al Trivelpiece
Director, Office of Energy
Research, U.S. DOE
M.S. 6E084
Washington, D.C. 20585

Mr. Marshal Tulin
Dept. of Mechanical Eng.
University of California
Santa Barbara, CA 93106

Dr. John F. Vesecky
Center for Radar Astronomy
233 Durand Building
Stanford University
Stanford, CA 94305

Mr. James P. Wade, Jr.
Prin. Dep. Under Secretary of
Defense for R&E
The Pentagon, Room 3E1014
Washington, D.C. 20301

Dr. Kenneth M. Watson
2191 Caminito Circulo Norte
La Jolla, CA 92037

Mr. Robert Winokur
Director, Planning & Assess.
Office of Naval Research
800 N. Quincy Street
Arlington, VA 22217

Mr. Leo Young
OUSDRE (R&AT)
The Pentagon, Room 3D1067
Washington, D.C. 20301

Dr. Fredrik Zachariasen (452-48)
California Institute
of Technology
1201 East California Street
Pasadena, CA 91125